

**DISPERSION OF BUOYANT LAGRANGIAN
PARTICLES IN THE WAVE-DRIVEN OCEAN
SURFACE BOUNDARY LAYER**

by

Kathleen Gamble

A thesis submitted to the Faculty of the University of Delaware in partial fulfillment of the requirements for the degree of Master of Science in Ocean Engineering

Summer 2018

© 2018 Kathleen Gamble
All Rights Reserved

**DISPERSION OF BUOYANT LAGRANGIAN
PARTICLES IN THE WAVE-DRIVEN OCEAN
SURFACE BOUNDARY LAYER**

by

Kathleen Gamble

Approved: _____
Tobias Kukulka, Ph.D.
Professor in charge of thesis on behalf of the Advisory Committee

Approved: _____
Mark A. Moline, Ph.D.
Director of the School of Marine Science and Policy

Approved: _____
Estella Atekwana, Ph.D.
Dean of the College of Earth, Ocean, and Environment

Approved: _____
Douglas J. Doren, Ph.D.
Interim Vice Provost for the Office of Graduate and Professional
Education

ACKNOWLEDGMENTS

Tobias Kukulka, Ph.D. for his continuous guidance and academic support over the past two years.

My parents, who have supported and helped me throughout my graduate education.

This work is supported by the National Science Foundation (Award number OCE-1352422), NOAA Delaware Sea Grant (Award number NA18OAR4170086), and a Marian R. Okie Fellowship. This research was also supported in part through the use of computational or staff resources provided by Information Technologies at the University of Delaware.

TABLE OF CONTENTS

LIST OF TABLES	v
LIST OF FIGURES	vi
ABSTRACT	vii
Chapter	
1 INTRODUCTION	1
1.1 Ocean Surface Boundary Layer Turbulence	1
1.2 Wave-Driven OSBL Turbulence	2
1.2.1 Langmuir Turbulence	2
1.2.2 Breaking Wave Effects	3
1.3 Modeling Approaches Based on Large Eddy Simulations (LES)	3
1.4 Modeling Buoyant Tracers	4
1.5 Purpose of Study	5
2 METHODOLOGY	7
2.1 Lagrangian Particle Tracking Overview	7
2.2 LES Resolved Scale model	8
2.3 Breaking Wave Model	10
2.4 Lagrangian Stochastic Model for Unresolved Motions	11
2.5 Experimental Runs	11
2.6 Particle Dispersion Analysis	13
3 RESULTS AND DISCUSSION	14
3.1 Flow Field Analysis	14
3.2 Particle Dispersion Overview	21
3.3 Particle Dispersion Analysis	27
3.3.1 Vertical Particle Distributions	27
3.3.2 Particle-Pair Distances	29
3.3.3 Horizontal Turbulent Diffusion Coefficient for Long Times	34
3.3.4 Principal Axes of Dispersion	38
4 CONCLUSION	40
REFERENCES	43

LIST OF TABLES

Table 2.1: Cases	13
------------------------	----

LIST OF FIGURES

Figure 3.1:	Mean velocity	15
Figure 3.2:	Mean velocity variance	17
Figure 3.3:	Total and SGS TKE	18
Figure 3.4:	3D turbulence snapshots	20
Figure 3.5:	Particle dispersion snapshots	25
Figure 3.6:	Example particle trajectories	26
Figure 3.7:	Concentration profiles	28
Figure 3.8:	Total mean distance squared	30
Figure 3.9:	Along-wind mean distance squared	31
Figure 3.10:	Crosswind mean distance squared	32
Figure 3.11:	Breaking wave initial dispersion	33
Figure 3.12:	Turbulence diffusion coefficients (x and y)	34
Figure 3.13:	OSBL schematic	37
Figure 3.14:	Turbulence diffusion coefficients (PC1 & PC2)	38

ABSTRACT

Upper ocean turbulence, generated by wind and wave forcing, directly controls air-sea exchange processes and the dispersion of material within the ocean surface boundary layer (OSBL). This study investigates the dispersion and transport of buoyant material, such as seaweed, phytoplankton, oil, and plastics, within the OSBL for varying buoyant rise velocities and wave conditions. Wave conditions studied include: shear turbulence, breaking wave (BW) effects, and Langmuir turbulence (LT). Breaking surface gravity waves transfer turbulent kinetic energy (TKE) into the ocean and result in enhanced TKE dissipation rates and mixing within a near-surface region. LT, captured by the Craik-Leibovich vortex force and other wave terms, results from interactions between the wave-driven Stokes drift and the turbulent current. LT is characterized by counter-rotating, near-surface vortices, which are a key for horizontal organization and submergence of buoyant particles. To model buoyant tracers in the turbulent OSBL, we employ a Lagrangian approach by tracking buoyant particles within a simulated OSBL flow field. The flow simulations are based on a large eddy simulation (LES) model coupled to a Lagrangian stochastic model, which captures particle velocities not resolved by the LES. Particle clouds are released at different vertical and horizontal positions and their dispersion characteristics quantified with probability density functions (e.g., concentration profiles) and the mean squared distance of particle pairs. In particular, we determine horizontal turbulent dispersion coefficients for dispersion times much larger than turbulent integral times. The initial dispersion of particle clouds depends on the local TKE dissipation rate and is nearly independent of buoyant rise velocity, consistent with the expected behavior for the inertial subrange. Enhanced TKE levels due to BW substantially increase initial dispersion rates. For longer time scales, both mean currents and turbulent eddies critically drive dispersion of buoyant particles within the OSBL. For small buoyant rise velocities, particle concentrations are transported vertically by turbulent eddies in all cases. Under shear turbulence conditions, sheared

mean currents differentially advect particle clouds with respect to depth, resulting in large turbulent diffusion coefficients for cases without LT. In contrast, enhanced vertical mixing due to Langmuir turbulence homogenizes currents with respect to depth, decreasing shear dispersion and, consequentially, turbulent diffusion coefficients for small buoyant rise velocities. When buoyant rise velocity is increased, small-scale shear and breaking wave turbulence are unable to efficiently submerge particle concentrations. This results in surface trapping of highly buoyant particles and significantly reduces shear dispersion and turbulent diffusion coefficients. Large Langmuir circulations, however, are still able to submerge highly buoyant particle concentrations, increasing horizontal dispersion. Results of this study indicate that dispersion of particles is highly dependent on both buoyant rise velocity and wave conditions. Therefore, both buoyant rise velocity and wave effects must be considered when modeling the transport of buoyant material within the OSBL.

Chapter 1

INTRODUCTION

1.1 Ocean Surface Boundary Layer Turbulence

The ocean surface boundary layer (OSBL), which varies in depth from several to a hundred meters, serves as an interface between the atmosphere and deep ocean. OSBL turbulence and air-sea fluxes play a critical role in weather and climate systems (Belcher et al, 2014; Sullivan and McWilliams, 2010; Thorpe, 2004). Furthermore, OSBL turbulence drives dispersion of buoyant material such as microplastic marine debris (Brunner et al, 2015; Kukulka and Brunner 2015), bubbles (Thorpe, 1982), nutrients and plankton (Denman and Gargett, 1995), and oil (Yang et al., 2015). This study investigates the dispersion of buoyant tracers in the OSBL, based on a computational particle tracking approach.

Upper ocean turbulence is generated through three primary mechanisms: wind forcing, wave forcing, and convection due to sea surface cooling. In this study, we do not consider the influence of convection. Wind forcing near the air-sea interface transfers momentum through wind stress to the upper ocean and drives OSBL currents, which decrease with depth. Flow instabilities form within this shear current, generating shear-driven turbulence. Energy transfer from wind forcing also drives surface gravity waves, determining the wave-driven Stokes drift and energy injected by breaking wave (BW) effects on OSBL turbulence are discussed in detail in the following subsection.

This study aims to investigate and quantify buoyant particle dispersion in the OSBL for varying wave conditions and buoyant rise velocity by applying a Lagrangian particle model based on a turbulence resolving three-dimensional flow model.

1.2 Wave-Driven OSBL Turbulence

1.2.1 Langmuir turbulence

Langmuir Turbulence (LT) is characterized as a near surface array of counter-rotating vortices. These vortices are approximately aligned with the wind and include nearly parallel zones of near-surface convergence and divergence. Zones of convergence at the ocean surface, termed windrows, accumulate buoyant debris (algae, seaweed, plastic, etc.) in linear patterns and indicate the formation of LT (Thorpe, 2004; McWilliams et al., 1997). Key features that characterize Langmuir turbulence within the OSBL include: sets of counter-rotating vortices approximately aligned with the direction of wind vector, strong downwelling bands aligned with converging crosswind velocities, and weak upwelling bands aligned with diverging crosswind velocities (Leibovich, 1983). Langmuir turbulence in the OSBL significantly enhances dispersion, transport, and mixing by altering turbulence and mixing characteristics within the OSBL (Belcher, 2012; Li et al., 2005; Thorpe, 2004).

A systematic theory for Langmuir turbulence generation, developed by Craik and Leibovich (1976), is based on the wave-averaged Navier-Stokes equations, called Craik-Leibovich equations. For the so-called CL2 mechanism, non-breaking waves interact with the turbulent currents through the Craik-Leibovich vortex force, which is the cross product between the Stokes drift velocity and vorticity, thereby generating Langmuir turbulence.

LT within the OSBL has been examined using observational methods such as: automated underwater vehicles (Thorpe et al., 2003), sidescan Doppler sonar (Smith et al., 1987), and floats/drifters (Farmer and Li, 1995). Through the use of freely drifting sonar deployed within the Strait of Georgia, Farmer and Li (1995) captured the evolution of bubble distributions and collective organization of distributions into Langmuir convergence lines. Bands of bubbles, resulting from the formation of Langmuir circulations within the OSBL, were further observed with acoustic sonar (Thorpe et al., 2003). Results of Thorpe et al. (2003) indicate that the largest

dissipation rate values occur within bubble clouds and are directly related to the presence of convergence zones due to LT formation.

1.2.2 Breaking Wave Effects

At the air-sea interface, momentum and energy from the wind is transferred to the wave field resulting in wave growth and eventual breaking of surface gravity waves (Phillips, 1977b). Breaking waves transfer energy to the OSBL. This process can be modeled as a flux of turbulent kinetic energy (TKE) vertically into the upper ocean (Craig and Banner, 1994). The Craig and Banner (1994) model captures enhanced near surface mixing and predicts TKE dissipation rate profiles that are consistent with measurements near the surface (Terray et al., 1996). Increased TKE from breaking surface waves, significantly enhances near-surface turbulence intensities and TKE dissipation rates, resulting in intensified near-surface mixing (Agrawal, 1992; Craig and Banner, 1994; Terray, 1996). For many conditions, these BW effects, likely only have significant direct effects on mixing near the ocean surface down to a depth that scales with significant wave height (H_s). The impact of breaking waves on buoyant particle dispersion will be investigated in this study.

1.3 Modeling Approaches Based on Large Eddy Simulation (LES)

Langmuir turbulence is commonly modeled using computational large eddy simulation (LES) models based on the Craik-Leibovich equations (Li et al., 2004; McWilliams et al., 1997; Denbo and Skillingstad 1995). LES models resolve larger scale turbulence that contributes most to TKE and turbulent fluxes but parameterize smaller scale turbulence. LES models capture many of the observed LT features, such as the formation of large coherent structures (upwelling and downwelling bands), converging crosswind surface velocities, and enhanced mixed layer deepening (McWilliams et al., 1997, Kukulka et al. 2009). LES results with LT effects have also been successfully compared to field observations of OSBL turbulence (Skillingstad et

al., 1999; Gargett et al., 2004; Li et al., 2009; Kukulka et al., 2009, 2011, 2012a, 2013; Harcourt and D'Asaro, 2010).”

There is not unified approach to incorporating breaking wave (BW) effects in LES models. Noh et al. (2004) and Li et al. (2013) simulate near-surface TKE injection due to BW effects through random surface forcing. Sullivan et al. (2004, 2007) simulate individual breaker evolution using stochastic breaking wave events. Results of both Sullivan et al. (2004, 2007) and Noh et al. (2004) are consistent with observational results of enhanced, near-surface TKE dissipation rates (Terray et al., 1996). Within this study, we will utilize an approach adopted from Kukulka and Brunner (2015) which specifies TKE as a surface TKE flux, which yields similar results to those obtained from more complex approaches. This method will be further discussed below within section 2.3.

1.4 Modeling Buoyant Tracers

Previous LES studies have simulated buoyant particles as tracer concentrations of constant buoyant rise velocity in the Eulerian framework to quantify dilution and concentration dispersion patterns of buoyant materials including: oil (Yang et al., 2014), microplastic marine debris (Kukulka and Brunner, 2015, Brunner et al. 2015), and bubbles (Liang et al, 2017). Buoyancy forces buoyant tracer concentrations towards the surface and plays a critical role in the distribution of particle concentrations with respect to depth. Yang et al. (2014) determines that the presence of Langmuir cells within the OSBL enhances the entrainment and dilution of oil concentrations. Yang et al. (2014) quantifies the ratio between LT effects and droplet buoyancy using a ratio of Stokes drift to droplet rise velocity. These results parallel findings by Kukulka and Brunner (2015) who note increased submergence of buoyant tracer concentrations for cases including Langmuir turbulence. Kukulka and Brunner (2015) additionally determine that effects of increased TKE, due to BW effects, remain confined to the near surface region and result in increased submergence of buoyant particle concentrations compared to shear turbulence.

In the Lagrangian framework, particles following the fluid motion are tracked with respect to both time and space. Pope (1994) and Sawford (2001) highlight the efficiency of Lagrangian approaches for understanding turbulent dispersion and mixing problems. Several studies have previously implemented particle tracking approaches for turbulent transport purposes in two-dimensional (2D) (Colbo and Li, 1999) and in three-dimensional (3D) form (Noh et al., 2006; Noh and Nakada, 2010; Liang et al., 2017; Kukulka and Veron, 2018). Results obtained by Colbo and Li (1999) are consistent with experimental observations collected using floating instrumentation/automated underwater vehicles (Farmer and Li, 1995; Thorpe et al., 2003) and indicate that buoyancy effects result in reduced crosswind dispersion of particle clouds in Langmuir circulations.

1.5 Purpose of Study

This study aims to utilize particle trajectories to analyze effects of buoyant rise velocity and wave conditions on both initial and long-term particle dispersion. The key question for this study is: How does total and horizontal particle dispersion depend on buoyant rise velocity and OSBL wave conditions?

The following hypotheses will be examined in this study:

Hypothesis 1: Shear turbulence will be ineffective in submerging buoyant particle concentrations but will result in larger horizontal dispersion than cases including Langmuir turbulence. Dispersion characteristics and statistics for this case will be especially dependent on buoyant rise velocity.

Hypothesis 2: Large, counter-rotating, coherent vortices, characteristic of Langmuir turbulence, will enhance submergence of particle concentrations but will inhibit horizontal dispersion of more buoyant particle clouds.

Hypothesis 3: Enhanced near-surface TKE and dissipation rates, resulting from BW effects, will enhance both horizontal and vertical dispersion of particle clouds located within the near-surface region.

Hypothesis 4: Dispersion of particle clouds is inversely related to buoyant rise velocity. If buoyant rise velocity is increased, surface trapping of particles will inhibit the ability of OSBL flow fields to disperse particle clouds effectively.

To address the key question and hypotheses, we utilize a coupled LES and Lagrangian stochastic model to track discrete particles within the turbulent 3D ocean surface boundary layer.

Chapter 2

METHODOLOGY

2.1 Lagrangian Particle Tracking Overview

Particles will be tracked in a turbulent 3D ocean. The Lagrangian particle tracking model employed for our study closely follows the approach by Kukulka and Veron (2018) that has been developed to understand basic effects of OSBL turbulence on particle dispersion and related time scales. Modifications have been made to the Kukulka and Veron (2018) particle tracking model to account for buoyancy effects. Our Lagrangian model is designed to track the trajectory ($\mathbf{X}(t, \mathbf{y})$) of n discrete particles located at position \mathbf{y} within the turbulent field by solving the governing equation:

$$\frac{d\mathbf{X}^n}{dt} = U_i^n (X_{j0}^n, t_0, t) \quad i = 1,2,3 \ \& \ j = 1,2,3 \quad (1)$$

where U_i^n is the Lagrangian particle velocity for the n^{th} tracer, t represents time, and X_{j0}^n is the particle release location at $t = t_0$. We define the position vector in the Eulerian reference frame as $\mathbf{x} = (x_1, x_2, x_3)$; where along-wind direction is represented by $x = x_1$, crosswind direction is $y = x_2$, and vertical direction is $z = x_3$ where $z = 0$ at the surface and positive upward. Applying this coordinate system, we further define the particle position as $\mathbf{X}^n = (X_1, X_2, X_3)$.

This study utilizes a rational turbulence resolving large eddy simulation of the OSBL coupled with a stochastic model modified from a previous Lagrangian particle study (Kukulka and Veron, 2018; Weil et al., 2004). Both resolved and sub-grid scale velocities, for each time point, are calculated and added, along with the Stokes velocity and buoyant rise velocities, to determine the total Lagrangian velocity acting on the tracers. The governing equation for the Lagrangian velocity can be written as follows (Kukulka and Veron 2018):

$$U_i^n (X_{j0}^n, t_0, t) = \bar{u}_i(\mathbf{X}^n, t) + u_i^{sgs}(\mathbf{X}^n, t) + u_{s,i}(\mathbf{X}^n, t) + w_b \delta_{i3} . \quad (2)$$

Within this equation, \bar{u}_i represents the resolved three dimensional LES velocity, u_i^{SGS} represents the unresolved subgrid scale (SGS) velocity of the LES, $u_{s,i}$ denotes the Stokes drift velocity, and w_b represents a constant vertical buoyant rise velocity. Resolved scale flow field velocities are determined based upon results of the LES model discussed below. Sub-grid scale velocities are modeled with a Lagrangian stochastic model and will be discussed further within section 2.4. This process for tracking particles must be completed for each discrete tracer and time step.

2.2 LES Resolved Scale Model

Results of the LES act as a basis for both the resolved and SGS flow fields utilized within the Lagrangian particle tracking model. The LES model for this study is adopted from McWilliams et al. (1997) with modifications to the SGS parametrization and the inclusion of non-monochromatic/breaking waves and Lagrangian buoyant tracer tracking methodology. Resolved and SGS velocity fields are calculated using spatially-filtered Navier-Stokes and continuum equations; where the filter length is set based on a pre-determined eddy viscosity value. The filtered Craik-Leibovich (1976) equation and respective governing density and continuity equations, solved within the LES code, can be written as (McWilliams et al., 1997):

$$\frac{\partial \bar{u}_i}{\partial t} + \bar{u}_j \frac{\partial \bar{u}_i}{\partial x_j} + \epsilon_{ikm} f_k (\bar{u}_m + u_{s,m}) = -\frac{\partial \bar{\pi}}{\partial x_i} + \frac{\bar{\rho}}{\rho_0} g_i + \epsilon_{ikm} u_{s,k} \bar{\omega}_m - \frac{\partial \tau_{ij}^{SGS}}{\partial x_j} \quad (3)$$

$$\frac{\partial \bar{\rho}}{\partial t} + (\bar{u}_j + u_{s,j}) \frac{\partial \bar{\rho}}{\partial x_j} = SGS \quad (4)$$

$$\frac{\partial \bar{u}_j}{\partial x_j} = 0 \quad (5)$$

Within these equations, the index $i = 1,2,3$ symbolizes along-wind, crosswind, and vertical directions; $u_i = (u_1, u_2, u_3)$ is the three dimensional velocity vector; $g_i = (0,0,-g)$ represents the gravitational acceleration where $g = 9.81 \text{ m/s}^2$; $f_k = (0,0,f)$ is the Coriolis force vector of magnitude $f = 10^{-4} \text{ s}^{-1}$; ϵ_{ikm} is the Levi-Civita permutation tensor; $\bar{\rho}$ is density; ρ_0 denotes a constant reference density; and π is a

generalized pressure written as $\pi = \frac{p}{\rho_0} + \frac{1}{2}[(u_i + u_{s,i})(u_i + u_{s,i}) - u_i u_i]$ (McWilliams et al., 1997; Kukulka, 2010). Overbars denote resolved flow field quantities. Interactions between the Stokes drift vector $(u_{s,1}, u_{s,2}, u_{s,3}) = (u_s, 0, 0)$ and resolved vorticity $(\overline{\omega}_m)$, which result in LT, are captured within the Craik-Leibovich vortex force (third right-hand-side term).

We parameterize unresolved turbulent scales through the use of the turbulent SGS momentum flux tensor (τ_{ij}^{SGS}) and SGS eddy viscosity (K_m). SGS eddy viscosity, (K_M), is calculated using the pre-determined spatial resolution ($l = (\Delta x \Delta y \Delta z)^{\frac{1}{3}}$), with Δx , Δy , and Δz representing grid resolution, and SGS turbulent kinetic energy (TKE).

$$\tau_{ij}^{SGS} = -K_m \left(\frac{\partial \overline{u}_i}{\partial x_j} + \frac{\partial \overline{u}_j}{\partial x_i} \right) \quad (6)$$

$$K_M = l e^{1/2} \quad (7)$$

Sub-grid scale turbulent kinetic energy (e) is calculated using the equation:

$$\frac{\partial e}{\partial t} + \overline{u}_j \frac{\partial e}{\partial x_j} = \tau_{ij}^{SGS} \frac{\partial \overline{u}_i}{\partial x_j} + \frac{g}{\rho_0} \tau_{\rho}^{SGS} + \frac{\partial}{\partial x_i} \left(2K_M \frac{\partial e}{\partial x_i} \right) - \epsilon + W(z) \quad (8)$$

Within equation 8, $W(z)$ represents the TKE contributed by breaking wave effects, discussed in the following subsection, τ_{ρ}^{SGS} represents the SGS density flux, and ϵ represents the turbulent dissipation rate. We calculate ϵ through the equation:

$$\epsilon = C e^{\frac{3}{2}} l^{-1}, \quad (9)$$

where C is a constant coefficient $C = 0.71$. The SGS equations implemented within this study are adopted from Kukulka and Brunner (2015) and respectively written above.

The Stokes drift is computed from an empirical wave height spectrum ϕ , following Kukulka and Brunner (2015)

$$\phi(\omega) = \alpha g^2 \omega^{-5} \frac{\omega}{\omega_p} \exp\left(-\left[\frac{\omega}{\omega_p}\right]^{-4}\right). \quad (10)$$

Within this equation, the parameter (α) can be written $\alpha = 0.006(\omega_p U_{10}/g)^{0.55}$. This spectrum is determined by two main input parameters, the wind speed at 10 m above the ocean surface (U_{10}) and the peak radian frequency (ω_p). In this study, we consider only fully developed seas with ($c_p/u_{*a} = 35$) for $U_{10} = 7$ m/s . Where c_p denotes the peak wave frequency and u_{*a} denotes the air-side friction velocity.

2.3 Breaking Wave Model:

One of the most significant changes within the SGS model is the addition of a TKE surface flux due to breaking waves in the horizontally averaged model. The methodology for incorporating breaking wave effects into the LES model of the OSBL is adopted from Kukulka and Brunner (2015). Breaking wave effects are incorporated as a horizontally uniform work term into the SGS turbulent kinetic energy equation and are equivalent to the total TKE flux from breaking waves. This vertically integrated work function is written:

$$\int_{-\infty}^0 W(z)dz = F \quad (11)$$

Furthermore, in wind-wave equilibrium conditions, the energy input into the upper ocean surface due to the breaking of waves (F) is approximately balanced by the total energy input from the wind; this balance is written:

$$F = g \int_0^{\omega_{max}} \beta \phi(\omega) d\omega \quad (12)$$

Where ω is the radian wave frequency, ϕ is the one-dimensional wave height frequency spectrum, and β denotes the wave growth rate approximated with Plant et al.'s (1982) empirical formula:

$$\beta = c_\beta u_*^2 c^{-2} \omega . \quad (13)$$

Within this equation, $c_\beta = (32 \pm 16)$ represents a nondimensional growth rate coefficient, $c = g/\omega$ is the wave phase speed, and $u_* = \sqrt{\tau/\rho_w}$ represents the water-side friction velocity. $\beta = 0$ for $\frac{c}{u_{*a}} > 35$, where $\frac{c}{u_{*a}}$ represents relative wave and wind speed. Air side friction velocity is denoted by u_{*a} . Wind stress, denoted by τ , is

directly related to wind speed by the drag coefficient parameterization: $\tau = C_D \rho_{air} U_{10}^2$ (Large and Pond, 1981). Within this equation, $C_D = 0.0013$ denotes a dimensionless drag coefficient and $\rho_{air} = 1.22 \text{ kg/m}^3$ denotes the density of air.

This work term dominates the sub-grid scale (SGS) turbulent kinetic energy (TKE) term and therefore directly increases the SGS eddy viscosity coefficient in equation (7) and, thus, turbulent SGS fluxes.

2.4 Lagrangian Stochastic Model for Unresolved Motions

Following Kukulka and Veron (2018), the sub-grid scale velocity is obtained from results of the parametrized LES SGS model coupled with the Lagrangian Stochastic Model (LSM) referenced within the particle dispersion model of Weil et al. (2004). The stochastic model for the sub-grid scale velocity (u_i^{sgs}), utilized to calculate particle position within our model, is written:

$$du_i^{sgs} = -\frac{C_0 \epsilon u_i^{sgs}}{2 \sigma_s^2} dt + \frac{1}{2} \left(\frac{1}{\sigma_s^2} \frac{d\sigma_s^2}{dt} u_i^{sgs} + \frac{\partial \sigma_s^2}{\partial x_i} \right) dt + (C_0 \bar{\epsilon})^{\frac{1}{2}} d\xi_i, \quad (14)$$

$$\sigma_s^2 = \frac{2e}{3}, \quad (15)$$

where σ_s^2 denotes the SGS velocity variance, and $d\xi_i$ is a normalized Gaussian random variable. Experimentally determined values for C_0 range between $C_0 = 4 \pm 2$ (Thomson, 1987) and $C_0 > 4$ (Pope, 2008). For this study we utilize a value of $C_0 = 6$, which is consistent with Pope (2008).

2.5 Experimental Runs

This study will consider four separate OSBL turbulence cases: shear turbulence (ST), shear turbulence and breaking waves (STBW), Langmuir turbulence (LT), and Langmuir turbulence and breaking waves (LTBW). Additionally, six separate buoyant rise velocities (w_b) will be studied ($w_b = 0.0, 0.2, 0.5, 1.0, 1.5, 2.1$ cm/s). Results for the $w_b = 0.2$ cm/s case are only shown if there is a clear difference between results for the $w_b = 0.5$ cm/s case. Buoyant rise velocities were chosen to reflect a broad range of buoyant particles from the neutrally buoyant case to largely

surface trapped cases, enabling us to understand dispersion behavior of wide ranges of buoyant material.

Our model setup is designed to accurately simulate realistic open-ocean OSBL turbulence conditions including Coriolis effects. Realistic wind and wave forcing conditions are adopted from Kukulka and Brunner (2015). Wind speed at 10m height above the ocean surface, U_{10} , is set to $U_{10} = 7$ m/s, which corresponds to a water-side friction velocity of $u_* = 0.0083$ m/s based upon the wind stress/ friction velocity relationship ($u_* = \sqrt{\tau/\rho}$). Within this equation, ρ denotes water density and τ represents wind stress. The computational domain for this model is $L_x = L_y = 150$ m in both horizontal directions and $h = 90$ m deep. The number of grid points in horizontal ($n_x = n_y = 128$) and vertical ($n_z = 300$) directions produce grid sizing sufficiently small to resolve energy-containing turbulent eddies.

Point sources, composed of 500 particles, are released at several locations at $t = 0$ seconds (as seen in Figure 6). Release locations include two separate depth levels (at the surface and at 3 m) and horizontal positions located within both convergence and divergence zones. These locations enable us to study the effects of breaking waves and small-scale Langmuir turbulence on initial point source dispersion. Cases considered for this study are outlined within Table 1 below.

OSBL case/ w_b	0.0 cm/s	0.2 cm/s	0.5 cm/s	1.0 cm/s	1.5 cm/s	2.1 cm/s
Shear turbulence (ST)	Case #1	Case #5	Case #9	Case #13	Case #17	Case #21
Breaking Waves (STBW)	Case #2	Case #6	Case #10	Case #14	Case #18	Case #22
Langmuir turbulence (LT)	Case #3	Case #7	Case #11	Case #15	Case #19	Case #23

Langmuir turbulence and Breaking waves (LTBW)	Case #4	Case #8	Case #12	Case #16	Case #20	Case #24
--	---------	---------	-------------	-------------	-------------	-------------

Table 2.1: Cases studied include four separate OSBL turbulence fields (ST, BW, LT, and LTBW) and five buoyant rise velocities ranging from neutrally buoyant to predominately surface trapped.

2.6 Particle Dispersion Analysis

Data collected from the cases referenced in Table 1 will be studied using several different methods. To both quantitatively and qualitatively understand dispersion of buoyant particle point sources, horizontal dispersion and vertical dispersion will be analyzed separately.

Horizontal mean particle-pair distance squared (d_i^2) statistics will be calculated with respect to both the x and y axes and axes rotated with respect to principal directions of dispersion, where PC1 denotes the major axis of dispersion and PC2 is the minor axis of dispersion. The mean-squared particle-pair distance along direction i is defined by:

$$d_i^2 = \left\{ (X_i - X_i')^2 \right\}. \quad (18)$$

Here $(X_i - X_i')^2$ represents the squared distance along i between two different particles located at X_i and X_i' and $\{ \}$ represents averaging for all particle pairs from a single point source.

Dispersion of particle clouds for sufficiently large times is similar to the ‘random walk’ behavior, described within Feynman et al. (1963), and can be characterized by the asymptotic law proposed by Taylor (1922) which describes particle dispersion with a constant turbulent diffusion coefficient,

$$A_i = \frac{1}{4} \frac{d(d_i^2)}{dt}. \quad (19)$$

Chapter 3

RESULTS & DISCUSSION

We will first provide an intuitive overview of flow fields and particle dispersion and then present an analysis of both horizontal dispersion and vertical distributions of buoyant particles in the turbulent OSBL. Subsection 3.1 provides an overview of flow field characteristics and statistics for our four OSBL turbulence cases (STBW, ST, LT, LTBW). The OSBL particle dispersion analysis is organized in two main sections: subsection 3.2 provides an intuitive overview of particle dispersion and trajectories within the OSBL, subsection 3.3 includes statistical analyses of dispersion in the vertical (3.3.1) and horizontal (3.3.2) directions.

3.1 Flow Field Analysis

Turbulence and sheared mean currents drive buoyant particle dispersion within the OSBL (Brunner et al, 2015; Kukulka and Veron, 2018). Thus, it is first critical to understand flow field characteristics and statistics for the four wave cases STBW, ST, LT, and LTBW. In particular, we examine a) profiles of mean horizontal velocities (Figure 1), b) profiles of resolved velocity variances (Figure 2), c) total and SGS TKE profiles (Figure 3), and d) instant three-dimensional snapshots of turbulent velocity fields, which illustrate the size and coherence of turbulent structures (Figure 4).

To understand how particles are advected within the OSBL, we analyze mean current profiles in the along-wind ($\langle u \rangle$) and crosswind ($\langle v \rangle$) directions (Figure 1). In ST and STBW cases, mean current profiles, for both along and crosswind directions, are sheared throughout the OSBL with large surface velocities that decay to zero at the base of the boundary layer. In contrast, mean current profiles for LT and LTBW cases are more uniform with respect to depth than are ST and STBW cases. We attribute more uniform mean current profiles to Langmuir circulations which significantly enhance vertical mixing within the OSBL. While LT and LTBW profiles are largely uniform with respect to depth, currents within a small region near the air-

sea boundary are highly sheared. Because BW effects are largely near-surface confined and small scale, mean current for STBW/ LTBW cases are similar to those of ST/ LT cases, respectively. Mean profiles produced within our study are consistent with results of previous LES studies (e.g., McWilliams et al., 1997).

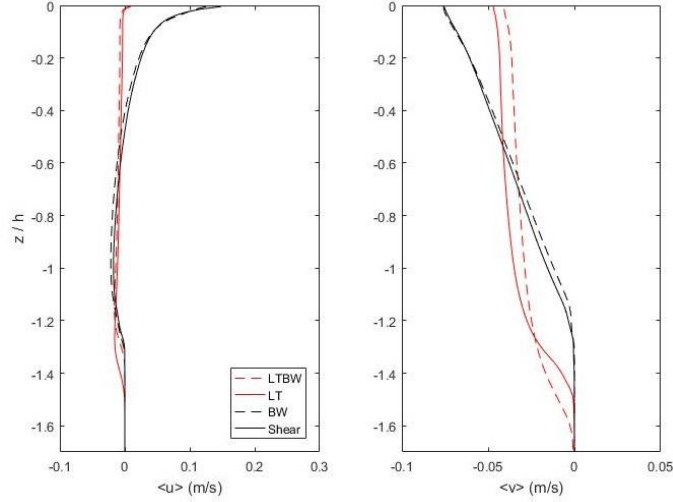


Figure 3.1: Time and horizontal mean velocity profiles in the along-wind ($\langle u \rangle$) and crosswind ($\langle v \rangle$) directions are shown with respect to depth. Solutions for shear turbulence, Langmuir turbulence, breaking waves, and Langmuir turbulence and breaking waves are included. Differences between LT and LTBW crosswind ($\langle v \rangle$) cases are contributed to differences in averaging procedure.

We next analyze and contrast resolved velocity variance profiles for the four different wave cases (Figure 2). These profiles are then related to turbulent structures revealed by three-dimensional (3D) snapshots of turbulent velocity fields. For shear (ST & STBW) cases, velocity variances follow the order: along-wind ($\langle u'^2 \rangle$) > crosswind ($\langle v'^2 \rangle$) > vertical ($\langle w'^2 \rangle$), consistent with expectations for ST (e.g., Li et al. 2004). Velocity variance profiles for shear cases change in shape with respect to direction. Shear profiles in the along-wind direction are largest at the surface and decay with depth, crosswind profiles are relatively uniform with respect to depth and eventually decay to zero below the OSBL, and vertical velocity profiles gradually

increase with respect to depth to a maximum around -0.2 then decay to zero. These near-surface regions of large along-wind velocity variance ($\langle u'^2 \rangle$) directly correspond to highly sheared, near-surface velocities present within the along-wind mean current profile (Figure 1). In contrast, velocity variance profiles for LT and LTBW cases follow the order: crosswind ($\langle v'^2 \rangle$) > vertical ($\langle w'^2 \rangle$) \approx along-wind ($\langle u'^2 \rangle$), as expected for LT (Li et al. 2004). LT along-wind ($\langle u'^2 \rangle$) and crosswind ($\langle v'^2 \rangle$) velocity variances are largest at the surface and rapidly decay with depth. Vertical velocity variance profiles for LT are similarly shaped to ST vertical velocity variance profiles but are significantly greater in magnitude with a large peak around -0.1. This indicates that downwelling, resulting from LT, is strongest slightly below the surface. Relatively large cross-wind velocity variance values near the surface are consistent with wind-aligned roll vortices with relatively strong divergent and convergent flows near the surface. Furthermore, significantly enhanced vertical LT velocity variance values are consistent with more uniform and well mixed mean current profiles. Resolved velocity variances for STBW and LTBW cases largely resemble those of shear turbulence and Langmuir turbulence cases, respectively, since small scale turbulent motions generated by BW's are not captured by resolved scales. These results are consistent with those of previous studies including McWilliams et al. (1997) and Li et al. (2004).

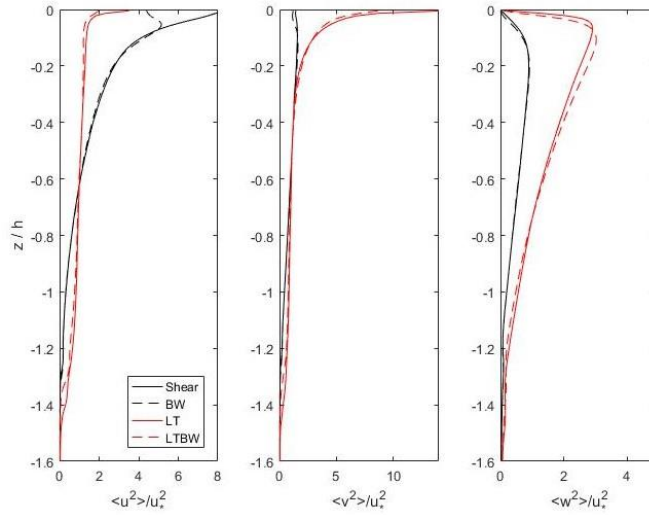


Figure 3.2: Time and horizontal mean vertical velocity variance profiles with respect to depth are shown for all directions ($\langle u'^2 \rangle, \langle v'^2 \rangle, \langle w'^2 \rangle$). ST, STBW, LT, and LTBW cases are all included.

While BW effects are not substantial within resolved mean current (Figure 1) and velocity variance profiles (Figure 2), significant differences between cases with and without BW are present within total TKE and SGS TKE profiles (Figure 3). Both LT and BW effects result in enhanced near-surface TKE values compared to the shear turbulence (ST) case. The largest total surface TKE values can be observed for STBW and LTBW cases. Furthermore, SGS TKE represents a larger portion of near-surface total TKE for cases including BW effects. These results are consistent with our BW modeling technique which parameterizes BW's as TKE fluxed vertically into the surface.

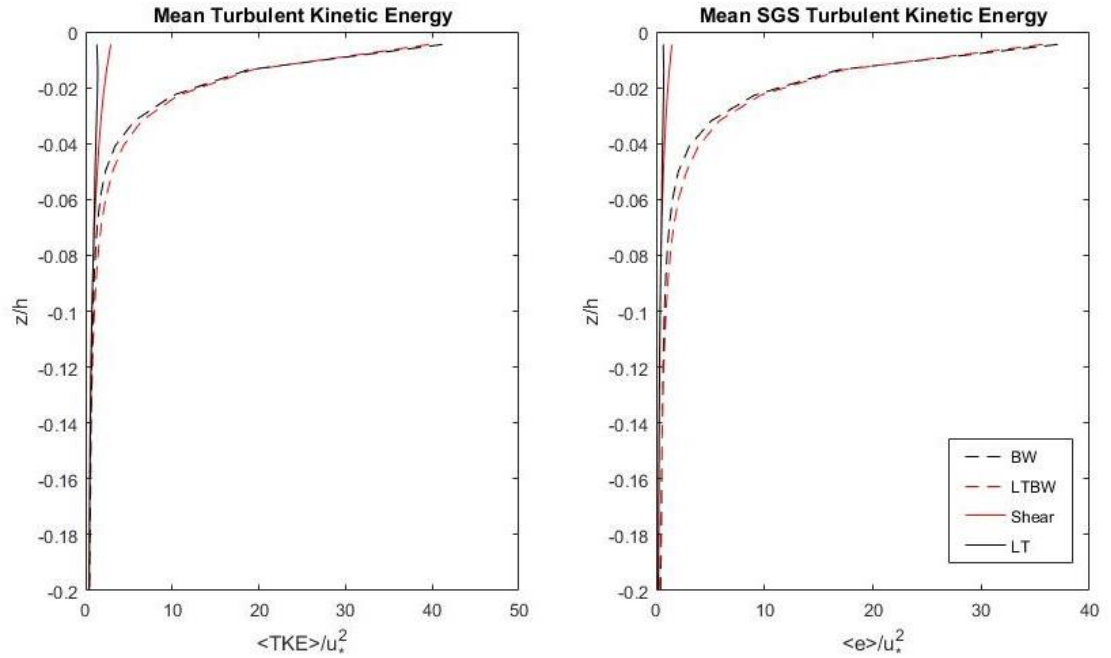


Figure 3.3: Time and horizontal mean TKE profiles are shown with respect to depth for all wave conditions (shear, BW, LT, LTBW). Cases including BW effects display significantly larger near-surface TKE values than shear and LT only cases.

Three-dimensional snapshots of the turbulent flow field, with mean currents subtracted, illustrate differences in turbulent flow characteristics and capture results observed within velocity variance profiles for varying wind-wave conditions (Figure 2). Large along-wind, near-surface velocity variances observed for ST and STBW cases can be related to small-scale, near-surface jets aligned observed within the along-wind ST and STBW 3D snapshots (Figure 4). Similarly, large crosswind and vertical velocity variances, observed for LT cases, directly correspond with coherent structures within LT and LTBW 3D snapshots (Figure 4). Large surface crosswind velocity variances directly correspond with strong coherent velocity structures observed within LT and LTBW crosswind 3D snapshots. Additionally, enhanced vertical velocity variances directly relate to downwelling and upwelling jets observed within LT and LTBW 3D vertical turbulence snapshots. Reduction of small-scale coherent structures and smoothing of large-scale structures is indicative of enhanced

mixing from BW effects and can be observed through direct comparison of 3D snapshots for ST/LT and STBW/LTBW cases in Figure 4.

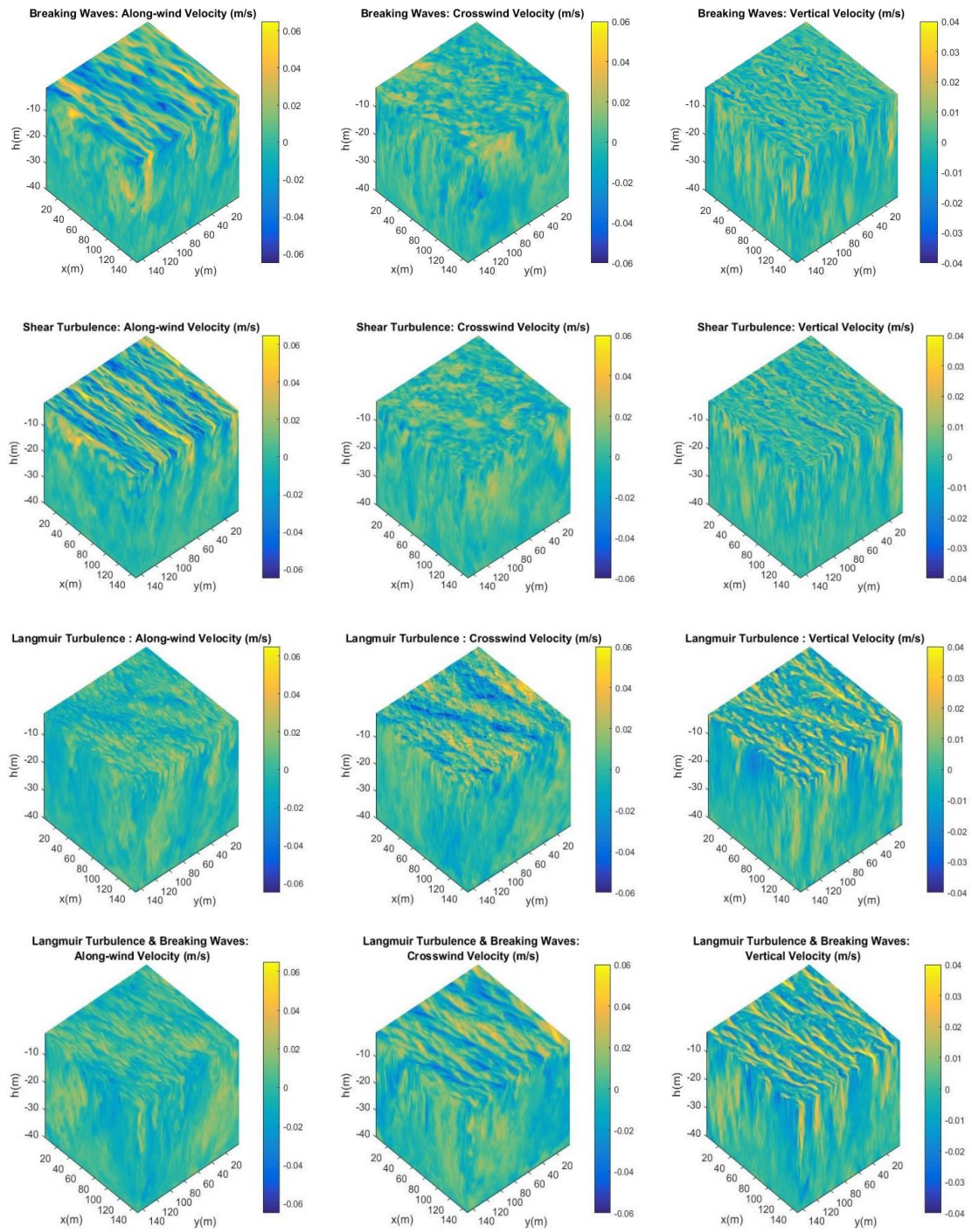


Figure 3.4: 3D turbulent velocity snapshots for all wind-wave cases. Includes along-wind, crosswind, and vertical velocities with the mean velocity removed to highlight

turbulence. Positive vertical velocities (yellow) indicate downwelling while negative vertical velocities (blue) indicate upwelling.

3.2 Particle Dispersion Overview

Snapshots of buoyant particle positions for different times (Figure 5) and particle trajectories (Figure 6) provide an intuitive overview of the evolution of particle motion and dispersion. Six separate buoyant rise velocities considered within this study range from neutrally buoyant ($w_b = 0.0$ cm/s) to highly buoyant ($w_b = 2.1$ cm/s). This range of w_b also includes the rise velocity of buoyant materials that exist within the ocean surface boundary layer (e.g., algae, plastic, zooplankton, nutrients, etc.). Figure 5 includes horizontal and vertical cross-section snapshots of buoyant particle dispersion under ST (5.a), STBW (5.b), LT (5.c), and LTBW (5.d) flow fields. Point sources are located at 6 separate locations along the crosswind (y) axis and two separate depths ($z = 0$ m, -3 m). We defined initial release locations to capture dispersion within both convergence and divergence regions for LT cases and near-surface breaking wave effects. Figure 6 shows initial ($t=20$ s) and long-term ($t = 15,000$ s) dispersion characteristics for particles of small ($w_b = 0.5$ cm/s) and large ($w_b = 2.1$ cm/s) buoyant rise velocities within ST, BW, LT, and LTBW flow fields.

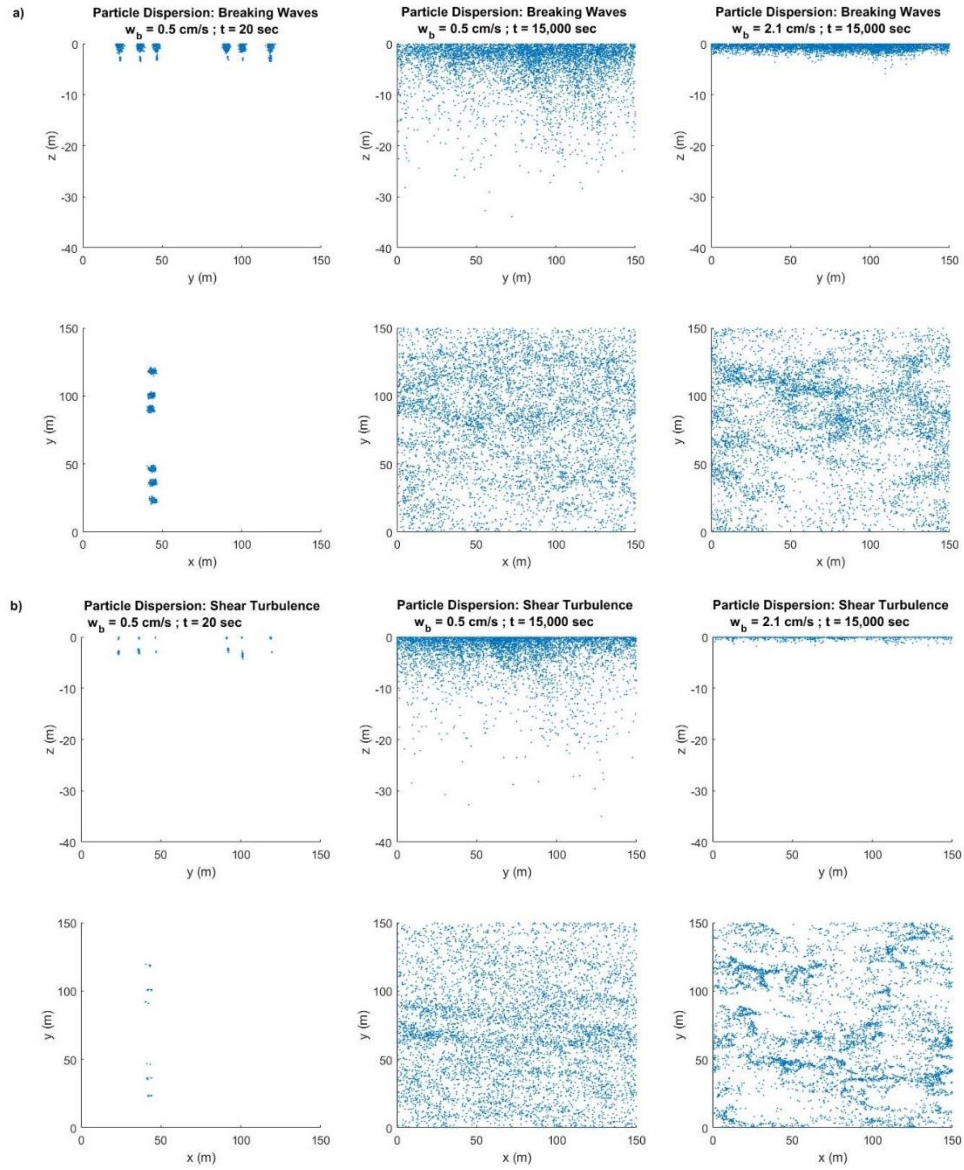
Initial particle dispersion, shown for $t = 20$ seconds, occurs in the inertial subrange and is characterized by the Richardson-Obukhov law which states that particle-pair dispersion, for times much smaller than the integral time scale, is directly related to both time and local turbulent dissipation rate (ϵ) (Sawford, 2001). Therefore, for small time scales, particle dispersion is largely dependent on local dissipation rates and consequently on the location of release. For cases that include breaking wave effects, initial dispersion of near-surface point sources is larger compared to point sources released at greater depths ($z = -3$ m) or within ST/ LT only cases (Figures 5.a, 5.d). This can be attributed to enhanced local near-surface TKE injection (Figure 3) and dissipation rates. For cases without BW effects, particle clouds generally remain compact initially and initial dispersion rates are smaller. In LT and LTBW cases, small

scale Langmuir structures locally enhance TKE and local dissipation rates within convergence zones (Thorpe, 2004). Enhanced TKE and dissipation rates in convergence zones result in enhanced initial dispersion of particle clouds (Figures 5.c, 5.d). Initial dispersion of particle clouds scale will be further discussed within subsection 3.3.

At larger times, buoyant rise velocity influences the vertical position of particles within the OSBL and therefore determines the scales of turbulent structures that drive dispersion. As buoyant rise velocity increases, particle concentrations are forced vertically towards the surface and eventually become surface trapped for very large rise velocities. Particles of small buoyant rise velocity, e.g., $w_b = 0.5$ cm/s, are effectively dispersed by larger-scale turbulence and mean currents. As w_b approaches zero, i.e. for the neutrally buoyant case, particle concentrations at sufficiently long time scales vertically homogenize (discussed in subsection 3.3.1). On the other hand, as buoyant rise velocity becomes larger, particles become increasingly trapped within the near-surface region of the OSBL. Organization of particle concentrations within the OSBL significantly impacts both horizontal and vertical dispersion. For strongly buoyant particles within shear turbulence only flow fields (Figure 5.b), vertical scatter of buoyant particles is largely reduced as small scale turbulent structures no longer efficiently transport particles. However, for LT and LTBW cases, enhanced vertical mixing due to the presence of Langmuir circulations, results in more efficient vertical transport of particles. Without LT, small scale turbulence generated by shear production is only able to submerge particles of small buoyant rise velocity to significant depths ($z = -30$ m). While LT enhances vertical scatter, converging near-surface crosswind velocities organize strongly buoyant particles in bands and significantly reduce horizontal scatter.

The inclusion of enhanced near-surface TKE from BW effects substantially increases submergence of near-surface particle concentrations compared to cases without BWs. Increased surface TKE injection due to breaking waves results in greater visual scatter of particle clouds, compared to the ST case, and near-surface

entrainment of surface trapped particle concentrations (Figure 5.a). However, horizontal and vertical dispersion of highly buoyant particle clouds (e.g., $w_b = 2.1$ cm/s) is still significantly reduced compared to cases of smaller buoyant rise velocity (Fig 5.a). Highly buoyant particles are much more efficiently submerged by large scale Langmuir structures than small scale structures present within shear or BW cases. These Langmuir circulations are critical for both horizontal organization and vertical transport of buoyant particles. Converging crosswind velocities due to counter-rotating Langmuir circulations, observable within Figure 4, horizontally organize buoyant particles into bands located in convergence zones (5.c, 5.d). Since convergence zones directly align with large downwelling velocities, surface trapped particles are still able to be submerged to depths between ten and twenty meters for both LT and LTBW cases. In addition to smoothing near-surface velocity structures (Figure 4), BW effects more efficiently mix near-surface concentrations and smooth coherent bands of particles trapped within Langmuir convergence zones (5.d).



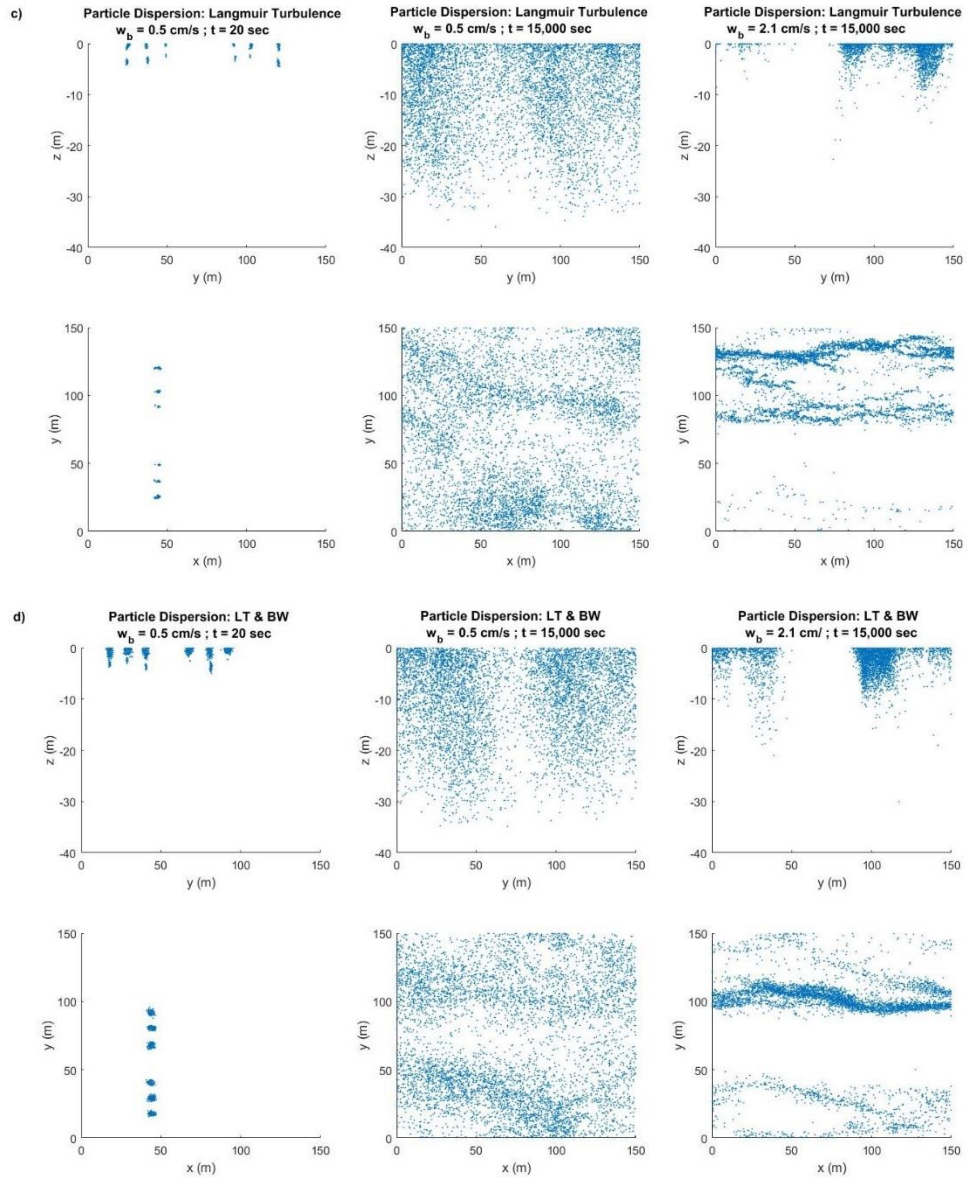


Figure 3.5: Horizontal and vertical cross-sections of particle dispersion are shown for flow field cases including: BW (5.a), Shear (5.b), LT (5.c), and LTBW (5.d). A small ($w_b = 0.5$ cm/s) and a larger ($w_b = 2.1$ cm/s) are shown for long term dispersion ($t = 15,000$ seconds) and dispersion for short times ($t=20$ seconds). Note that only results for one buoyant rise ($w_b=0.5$ cm/s) are shown for the initial dispersion since dispersion rates at times much smaller than the integral time scale are nearly independent of buoyant rise velocity.

Lagrangian particle motion and dispersion can be further illustrated through example particle trajectories (Figure 6). Figure 6 illustrates that large, energy-carrying coherent Langmuir circulations critically affect vertical movement of buoyant particles. In cases that include LT, both the magnitude and frequency of particle submergence is increased. Without LT, particle trajectories remain largely confined within ten meters of the surface. Rapid vertical oscillation of example STBW/LTBW particle trajectories (Figure 6), between the surface and a depth of a few meters, is indicative of higher frequency movement caused by enhanced near-surface TKE injection from BWs (Figure 3). These particle trajectories and the particle snapshots suggest that buoyant rise velocity and wave effects strongly influence particle dispersion.

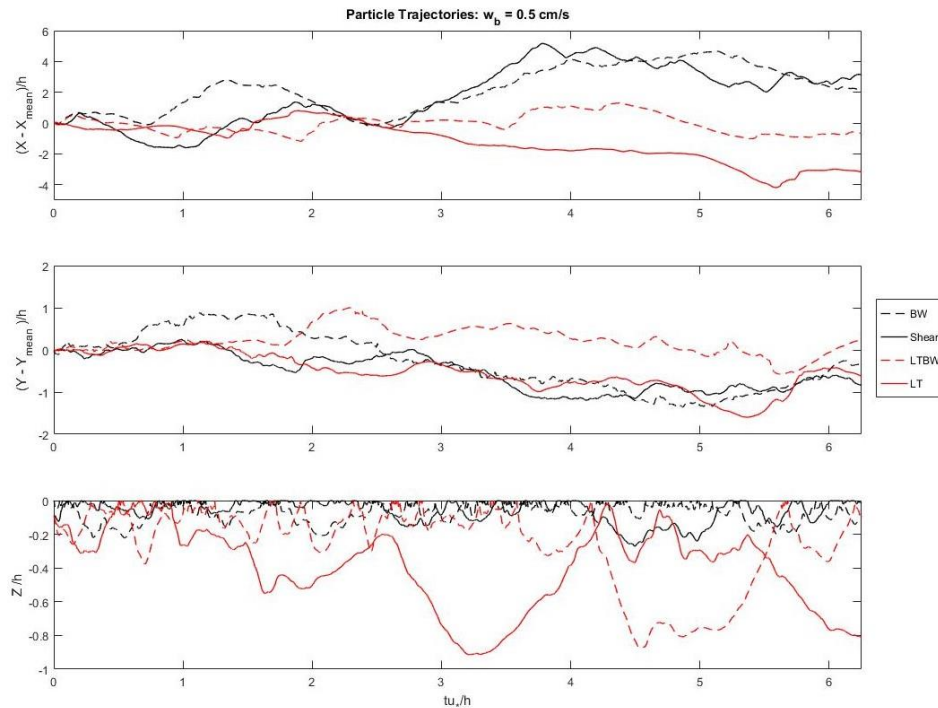


Figure 3.6: Example particle trajectories are shown for a buoyant rise velocity of 0.5 cm/s. Trajectories are calculated with the mean position subtracted. BW (black dashed), Shear (black), LT (red), and LTBW (red dashed) cases are shown for all directions vs. a normalized time scale (tu_*/h); where $u_* = 0.0083$ m/s and $h = 33$ m.

3.3 Particle Dispersion Analysis

One of the primary objectives of this study is to understand the effects of varying wave cases (ST, STBW, LT, LTBW) and buoyant rise velocity on particle dispersion from short to long times relative to the turbulent integral time. Subsection 3.3 is further broken down into two separate sections: vertical distributions (3.3.1) and horizontal dispersion (3.3.2). Analysis of both vertical and horizontal particle cloud dispersion statistics is critical for determining what processes drive dispersion for different wave and buoyancy cases. Vertical distributions of particle concentrations dictate what mean sheared currents and turbulence drive particle dispersion. For instance, surface trapped particles are advected by the turbulent surface current, while homogeneously submerged particle concentrations are transported by turbulent currents throughout the OSBL.

3.3.1 Vertical Particle Distributions

To effectively analyze turbulent dispersion for all buoyant rise velocities and wave effects, we must first understand how particle concentrations are organized with respect to depth for all cases. Both buoyant rise velocity and vertical turbulence dictate the position with respect to depth of buoyant particles (Kukulka and Brunner 2015). Vertical location of concentrations within the OSBL determines what currents and turbulence scales advect and disperse particles. Normalized particle concentration profiles are plotted below with respect to depth for all buoyant rise velocity and wind-wave conditions (Figure 7).

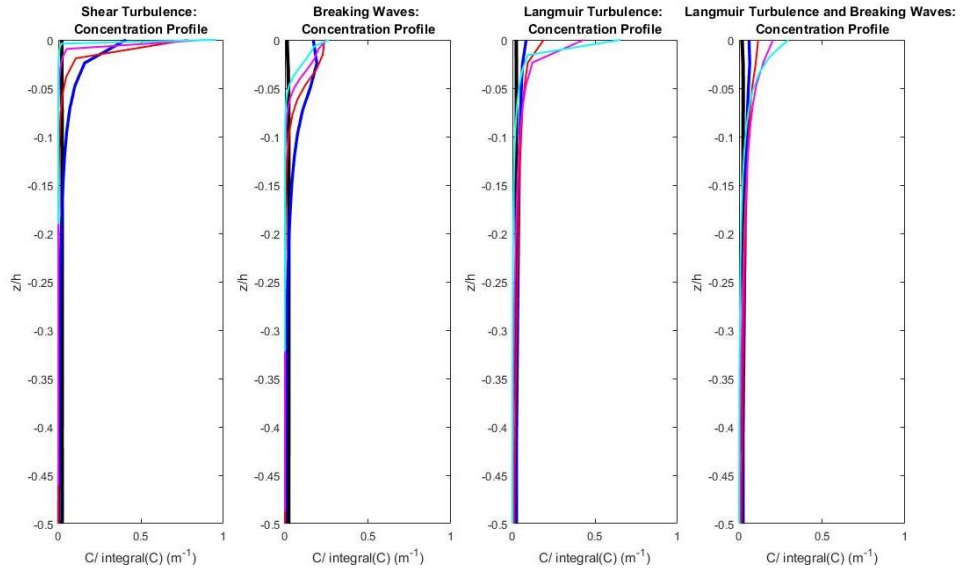


Figure 3.7: Normalized concentrations C with respect to depth are shown for buoyant rise velocities of 0.0 cm/s (black), 0.5 cm/s (blue), 1.0 cm/s (red), 1.5 cm/s (magenta), and 2.1 cm/s (cyan). Depth is normalized by mixed layer depth ($h = 33\text{m}$).

Concentration profiles are calculated only for longer time scales. The total (depth-integrated) concentration is denoted by “integral(C)” which equals $\int_{-h}^0 C(z) dz$.

For neutrally buoyant particles ($w_b = 0.0$ m/s), concentrations are vertically homogenous with respect to depth for all cases. As buoyant rise velocity is increased, particle concentrations become progressively trapped within the near-surface region of the OSBL. Even small buoyant rise velocities, e.g., $w_b = 0.5$ cm/s, shift particle concentrations toward the surface compared to homogeneously distributed neutrally buoyant concentrations. The extent of surface trapping of concentrations, for each buoyant rise velocity, varies in magnitude with respect to wave conditions. In the case of shear turbulence, small turbulent structures generated by shear production are unlikely to submerge particles of buoyant rise velocities larger than 1.0 cm/s. Increased near-surface TKE and dissipation rates due to the inclusion of breaking wave effects submerge concentrations to greater depths than shear turbulence.

Enhanced vertical mixing due to Langmuir turbulence additionally submerges surface particles and reduces near surface concentrations. The combination of increased near surface TKE from BWs and enhanced vertical mixing due to LT results in the largest submergence of highly buoyant particles of all cases. TKE injection due to BWs can force surface trapped particles into regions of large downwelling velocity within LT convergence zones, directly enhancing the ability of LT to deeply submerge buoyant particles (Figure 7). Therefore, particle concentration profiles, coupled with mean sheared current and velocity variance profiles, provide insight into driving mechanisms of long-term buoyant particle dispersion for varying buoyant rise velocity and OSBL wave condition cases.

3.3.2 Particle-Pair Distances

We statistically describe buoyant point source dispersion using the mean-squared particle-pair distance, which is effective for characterizing the evolution of particle point sources (e.g., Sawford (2001)) and has recently been applied to study wave-driven OSBL turbulence (Kukulka and Veron, 2018). We utilize equation 18 to calculate the total mean particle-pair distance squared, $d^2 = d_1^2 + d_2^2$ (Figure 8), along-wind particle-pair distance squared, d_1^2 (Figure 9), and crosswind particle-pair distance squared, d_2^2 (Figure 10) and plot these results with respect to time.

Different point source release locations enable the analysis of how depth and crosswind position affect particle dispersion statistics. Particle clouds were released at two separate depth levels (at the surface and at $z = -3$ m) and at six horizontal positions located within convergence and divergence zones. Mean particle-pair distance squared results are displayed only for one location released at the surface. Long-term behavior is independent of release location and therefore results are only shown for one location.

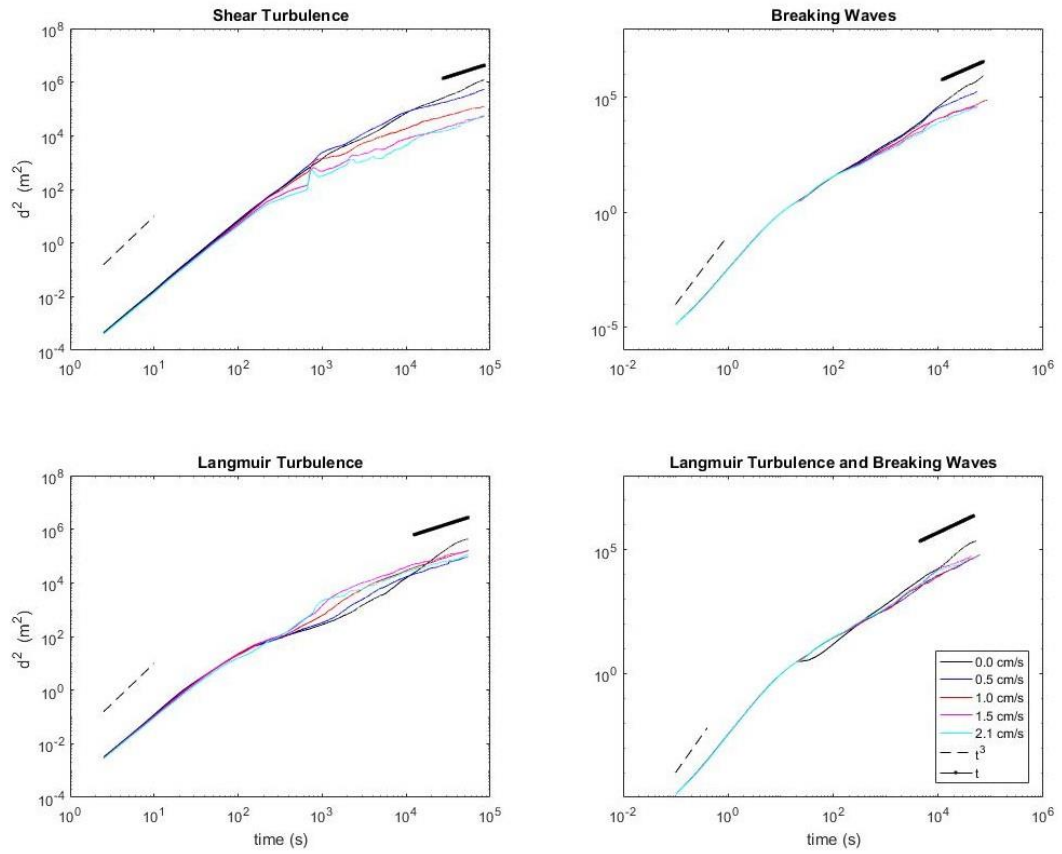


Figure 3.8: The total mean distance squared d^2 in m^2 for surface release locations, is shown for five buoyant rise velocity cases ($w_b = 0.0$ cm/s, 0.5 cm/s, 1.0 cm/s, 1.5 cm/s, 2.1 cm/s). Mean particle-pair distance squared results for times much smaller than the integral time scale and times much greater than the integral time scale converge to Richardson-Obukhov (small times) and Taylor (long time) asymptotic limits.

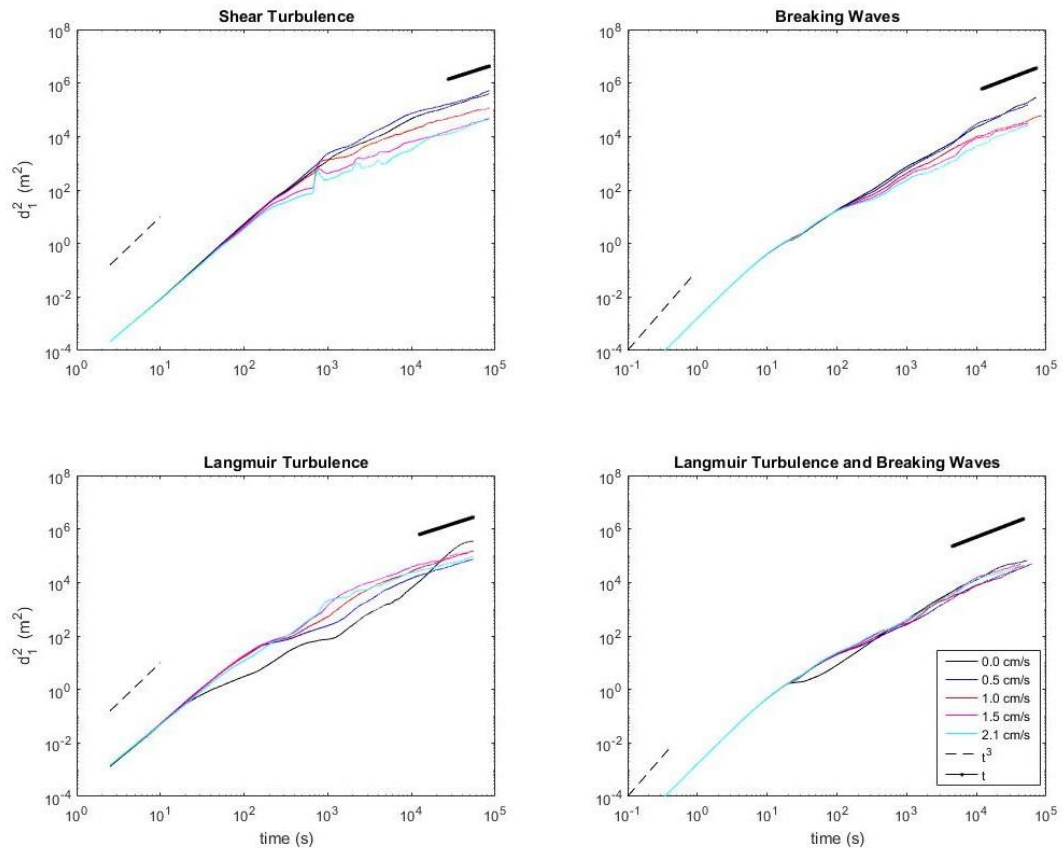


Figure 3.9: Along-wind dispersion of point sources, d_1^2 (m^2), for surface release locations, is shown for five buoyant rise velocity cases ($w_b = 0.0$ cm/s, 0.5 cm/s, 1.0 cm/s, 1.5 cm/s, 2.1 cm/s). Mean particle-pair distance squared results for times \ll integral time scale and times \gg integral time scale converge to Richardson-Obukhov (small times) and Taylor (long time) asymptotic limits.

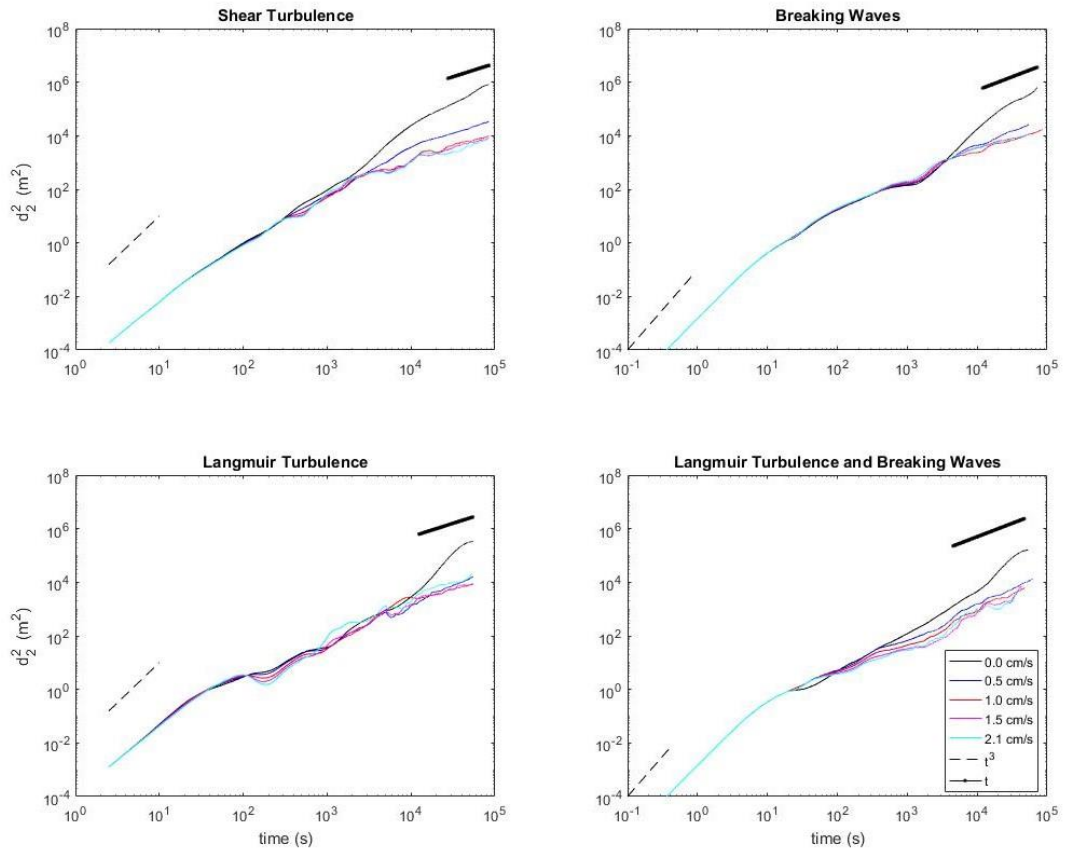


Figure 3.10: Crosswind dispersion of point sources, $d_2^2(m^2)$, for surface release locations, is shown for five buoyant rise velocity cases ($w_b= 0.0$ cm/s, 0.5 cm/s, 1.0 cm/s, 1.5 cm/s, 2.1 cm/s). Mean particle-pair distance squared results for times \ll integral time scale and times \gg integral time scale converge to Richardson-Obukhov (small times) and Taylor (long time) asymptotic limits.

Total and horizontal mean particle-pair distance squared plots capture key characteristics of turbulent dispersion. For initial dispersion, mean particle-pair distance results converge to the expected Richardson-Obukhov law with distance square proportional to t^3 (Sawford, 2001) and are approximately independent of buoyant rise velocity. Furthermore, enhanced initial near-surface dispersion of point sources due to increased BW surface dissipation rates is captured. Figure 11 compares the total mean particle-pair distance squared results for a surface released ($z = 0$ m)

point source to results for a point source released at greater depths ($z = -3$ m). For sufficiently small times, mean distance squared values for surface released cases are two orders of magnitude larger than those of the point source released at larger depths or point sources for cases without BW effects. Differences in initial dispersion can be attributed to enhanced BW TKE and dissipation rates at near-surface regions (Figure 3).

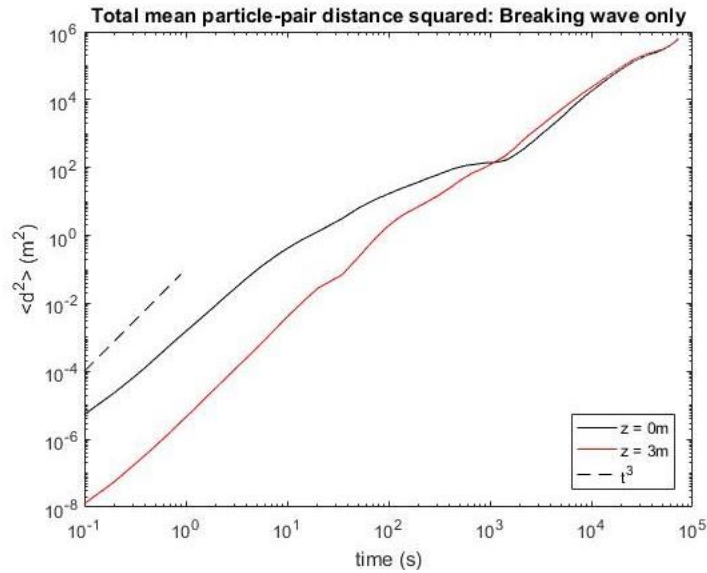


Figure 3.11: Total dispersion of point sources under breaking waves, $d^2(m^2)$, for a surface release location ($z = 0\text{m}$) and one at larger depths ($z = 3\text{m}$), is shown. Mean particle-pair distance squared results for times \ll integral time scale converge to Richardson-Obukhov (small times) and are magnitudes larger for surface released point sources.

For intermediate and long times, mean particle-pair distance squared values are controlled by larger-energy containing eddies and mean currents. During the intermediate time range, d_i^2 values increase at varying rates and occasionally decrease. This is attributed to the presence of large coherent vortices, primarily within LT cases, that result in stretching and compressing of particle clouds without necessarily resulting in mixing. At sufficiently long times, d_i^2 behavior is statistically governed by

the asymptotic law described by Taylor (1922). Within section 3.3.3, we utilize Taylor analysis to characterize long-term dispersion for varying buoyant rise velocity and wave conditions.

3.3.3 Horizontal Turbulent Diffusion Coefficient for Long Times

To further understand how varying wave conditions and buoyant rise velocity affect buoyant particle dispersion, we utilize mean particle-pair distance squared results (Figures 8 to 11) to analyze long-term particle cloud dispersion. For times much larger than the turbulent integral time scale, particle dispersion is analogous to a ‘random walk’ (Taylor 1922), so that horizontal turbulent diffusion coefficients can be determined by equation 19. This is discussed in subsection 2.6 for the total distance squared ($A = A_1 + A_2$), in the along-wind direction (A_1), and crosswind direction (A_2). We discuss results for total (A), along-wind (A_1), and crosswind (A_2) turbulent diffusion coefficients (Figure 12) for each buoyant rise velocity, beginning with the neutrally buoyant case, and provide interpretations of results on a case by case basis.

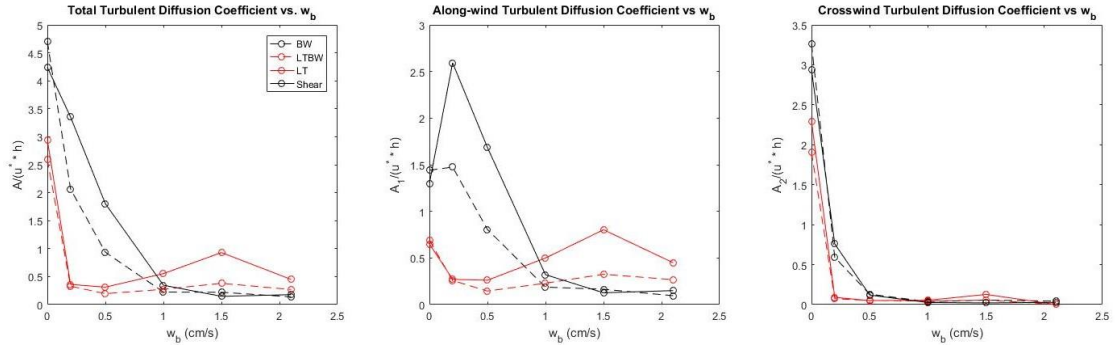


Figure 3.12: Turbulence dispersion coefficients are plotted vs. buoyant rise velocity for ST (black), STBW (black dashed), LT (red), and LTBW (red dashed) cases.

Coefficients are normalized by $(u_* h)$ where $u_* = 0.0083 \text{ m/s}$ and $h = 33\text{m}$.

For neutral and small buoyant rise velocities, ST/STBW turbulent diffusion coefficients are larger than those of LT/LTBW cases and decrease rapidly as buoyant rise velocity is increased. At an intermediate buoyant rise velocity of $w_b = 1.0 \text{ cm/s}$, the ordering of turbulent diffusion coefficients begins to change with Langmuir

turbulence cases overtaking ST/STBW cases in magnitude. As this buoyancy further increases, LT/ LTBW turbulent diffusion coefficients are larger than those for ST and STBW cases. For most cases, BWs decrease turbulent diffusion coefficients. Diffusion coefficient converge to a constant value for large w_b as particles become surface trapped.

We interpret these results using: mean velocity (Figure 1), velocity variance (Figure 2), TKE (Figure 3), and concentration (Figure 7) profiles. Diffusion coefficients for the neutrally buoyant case are significantly larger in magnitude than those of small buoyant rise velocities (Figure 12). Since neutrally buoyant particles are vertically transported throughout the whole OSBL in all cases, relatively large turbulent diffusion coefficients are due to enhanced dispersion of particles by large eddies and shear at the surface and base of the OSBL (Figure 13). Particle trapping below the mixed layer may also contribute to enhanced diffusion coefficients as those particles are not advected by currents potentially enhancing differential advection and associated shear dispersion. Vertically sheared currents, within ST and STBW cases (Figure 1), transport particles differentially, depending on the particle's depth location, which results in horizontal dispersion, referred to as shear dispersion. The larger the shear is, and the more particles located in sheared flow, the greater the dispersion rate due to vertically sheared currents. Differences between ST/ STBW coefficients are likely attributed to enhanced trapping of neutrally buoyant particles below the mixed layer due to BW effects. The presence of LT within the OSBL results in more uniform mean currents and, consequently, reduced shear dispersion. Furthermore, results for our neutrally buoyant case indicate that BW effects enhance dispersion of neutrally buoyant particle clouds compared to cases without breaking wave effects. This is not so for the LT case and may be attributed to disruption of small scale LT structures by BW effects (Kukulka and Brunner, 2015)

Results from our study show that, for cases of small buoyant rise velocity (e.g., $w_b = 0.2$ cm/s, 0.5 cm/s), turbulent diffusion coefficients are decreased with respect to the neutrally buoyant case. Small changes in buoyant rise velocities result in

substantial changes in magnitude of turbulent diffusion coefficients, indicating that varying w_b results in sampling of different flows for each case. This can be attributed to particle concentrations becoming more surface concentrated and less likely to be trapped or dispersed by larger eddies/ sheared currents at the base of the OSBL (Figure 7), schematically shown in Figure 13. Neutrally buoyant concentrations, represented by the black dashed line within Figure 13, sample small and large eddies in addition to the full mean current, including sheared regions near the surface and base of the OSBL. As buoyant rise velocity is slightly increased, concentrations are forced towards near-surface regions (red line figure 13), resulting in sampling of only the upper mean current. Furthermore, this result is consistent with results obtained by Colbo and Li (1999) which determined that buoyancy effects significantly inhibit crosswind dispersion of particle clouds within LT flow fields. For smaller buoyant rise velocities, particle concentrations are transported vertically by turbulent eddies in all cases (ST, STBW, LT, LTBW) and horizontal particle dispersion is predominately controlled by larger turbulent eddies sheared currents shown.

As buoyant rise velocities further increase, the order in magnitude of turbulent diffusion coefficients begins to shift. We attribute this change in turbulent diffusion coefficients to the fact that, without LT, highly buoyant particles are no longer efficiently transported vertically and become increasingly trapped within the near-surface region, which is schematically represented by the blue concentration profile in Figure 13. With LT, coherent Langmuir structures (small and larger scale as schematically represented in Figure 13) are critical in deeper submergence. With LT, a significant number of particles remain surface trapped within convergence zones (Figure 5); nevertheless, strong downwelling velocities underneath convergence regions are able to submerge particles (represented schematically by the red concentration profile) and expose concentrations to relatively strong shear (idealized current profile shown by black line in Figure 13) resulting in more efficient dispersion.

The presence of BWs generally results in decreased turbulent diffusion coefficients. It is somewhat counter-intuitive that BWs reduce horizontal dispersion

for both ST and cases. One possible explanation is that BWs disrupt small scale coherent structures (represented by small near-surface eddies in Figure 13) that efficiently disperse material (Kukulka and Brunner, 2015).

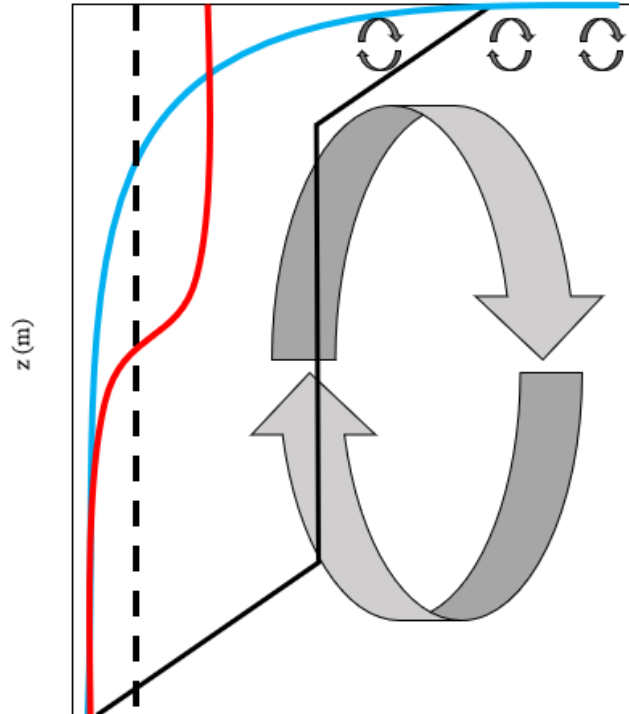


Figure 3.13: A simple schematic of particle dispersion within the OSBL is shown for: neutrally buoyant particles (black-dashed), intermediate buoyancy particles (red), and highly buoyant particles (light blue). A simplified mean current is shown with regions of shear near the surface and base of the OSBL. Small and large eddies are also included.

Additionally, turbulent diffusion coefficients for along-wind (A_1) and crosswind (A_2) directions are analyzed. Except for the neutrally buoyant case ($w_b = 0.0$ cm/s), along-wind turbulent diffusion coefficients (A_1) are similar to total dispersion coefficients and are substantially larger than crosswind diffusion coefficients (A_2). For $w_b = 0.0$ cm/s, crosswind diffusion coefficients, A_2 , are closer to total diffusion coefficients and are larger in magnitude than coefficients computed for

the along-wind direction. To further examine the direction of dispersion, we will next investigate the principal axes of dispersion for each case.

3.3.4 Principal Axes of Dispersion

It is also important to consider that the along-wind and crosswind axes are generally not the principal axes of dispersion because the currents and current shear turn with depth. The LES model for this study is designed to accurately simulate open ocean OSBL turbulence, with the inclusion of a Coriolis force. For the Ekman layer with positive f , this results in the depth integrated mean currents being aligned to the right-hand side of the wind direction.

To address this issue, major (PC1 = $(x_{1,PC1}, x_{2,PC1})$) and minor (PC2) principal axes of dispersion were calculated using particle positions for each cloud at times much larger than the integral time scale. This was done for all buoyant rise velocities ($w_b = 0.0$ cm/s, 0.2 cm/s, 0.5 cm/s, 1.0 cm/s, 1.5 cm/s, and 2.1 cm/s) and OSBL turbulence conditions (ST, STBW, LT, LTBW). Mean particle-pair distance squared values were recomputed along the principal axes and then utilized to calculate turbulent diffusion coefficients along the principal axes for each case. Angle of dispersion with respect to the wind and turbulent diffusion coefficients are plotted with respect to buoyant rise velocity and shown below for all cases (Figure 14).

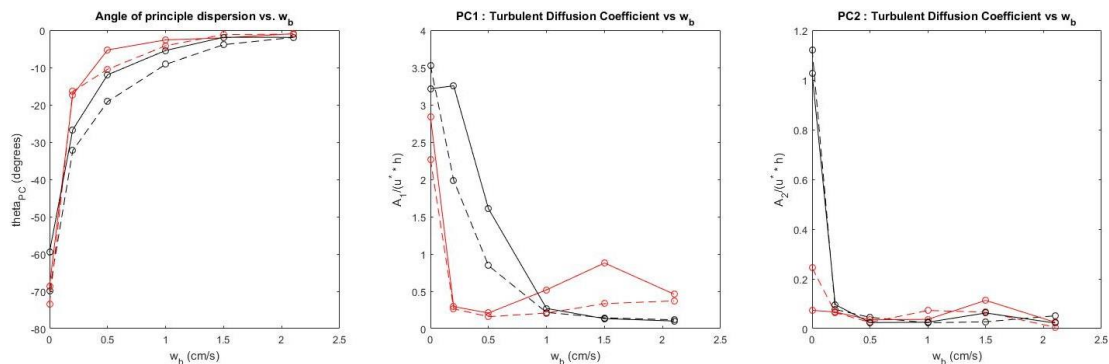


Figure 3.14: Both the angle of principle dispersion and turbulent diffusion coefficients for both principle axis are plotted versus buoyant rise velocity. Cases include BW (black dashed), Shear (black), LT (red), and LTBW (red dashed) for all buoyant rise

velocities. Coefficients are normalized by (u_*h) . Here A1 is along PC1 and A2 is along PC2.

The angle between the x axis and the major principal axis is given by $\theta_{PC} = \arctan\left(\frac{x_{2,PC1}}{x_{1,PC1}}\right)$. The major principal axis for cases of small buoyant rise velocity is significantly misaligned with the x and y axes. These significant misalignments can most likely be attributed to the fact that particles of smaller buoyant rise velocities are more homogeneously distributed in the vertical direction. Thus, the direction of particle dispersion is affected by the Ekman spiral (Figure 3). As buoyant rise velocity is increased, and particles become increasingly surface trapped, the angle of principle dispersion begins to align more closely with wind direction. This alignment can most likely be attributed to the organization of surface trapped particles within strong, along-wind near surface shear jets and LT convergence zones, which approximately align with the direction of wind forcing (x-axis). Our results suggest that sheared along-wind jets, characteristic of Langmuir circulations (Kukulka et al., 2010; Polton et al., 2005; Weller et al., 1985), advect near-surface particle concentrations trapped within convergence zones in the wind direction and approximately align the primary direction of dispersion with the wind.

Additionally, turbulent diffusion coefficients for both PC1 and PC2 primarily follow the same trends and characteristics as for x and y axes. These results indicate that the direction of point source dispersion is dependent on both buoyant rise velocity, OSBL turbulence, and wave conditions. Therefore, it is critical to analyze dispersion along the principle axes in addition to analyzing dispersion with respect to traditional axes.

Chapter 4

CONCLUSION

Based on a Lagrangian particle tracking approach, we have analyzed point source dispersion for varying OSBL wave conditions and buoyant rise velocities. This study examines a wide range of buoyant rise velocity values ranging from the neutrally buoyant case, previously studied by Kukulka and Veron (2018), to a largely surface trapped case. This was done to gain insight into how a wide variety of buoyant materials disperse such as: plastic, zoo plankton, nutrients, harmful chemicals, etc. Results are based on a 3-dimensional time-dependent turbulence resolving LES model coupled with a Lagrangian stochastic model. Flow fields and velocity profiles derived from this LES model reveal key differences between four OSBL wave condition for which turbulence is driven by shear (ST case), and Langmuir turbulence (LT case), and breaking waves with LT (LTBW case) and without (STBW case). Wind-driven shear currents generate small but energetic turbulent structures and result in a highly sheared mean velocity profile with respect to depth. Interactions between instabilities produced by the turbulent current and wave-driven Stokes drift, result in the formation of counter-rotating vortices, approximately aligned with the wind, that characterize Langmuir turbulence and are described by the CL2 mechanism (Craig and Leibovich, 1976). These Langmuir circulations organize and disperse particles in both the horizontal and vertical planes in the crosswind and vertical directions. Enhanced vertical mixing and transport due to LT results in a more uniform mean current with respect to depth compared to highly sheared mean currents for ST and STBW cases. Breaking wave effects, modeled as a surface TKE flux into the ocean surface, increase near-surface TKE and TKE dissipation rates

In order to better analyze how particle clouds disperse, we statistically describe point source dispersion using both mean distance particle-pair squared values and turbulent diffusion coefficients. Mean particle-pair squared distances were evaluated for both initial and long-term dispersion, initial dispersion being characterized by the

Richardson-Obukhov law (Sawford, 2001) and dispersion for times much larger than the integral time scale being characterized by Taylor dispersion (1922). Since TKE injection due to breaking waves enhances near surface dissipation rates, initial dispersion of near-surface particle clouds released at the surface in BW cases was significantly larger compared to both LT and shear only cases.

For long times, we determined horizontal turbulent diffusion coefficients based on Taylor's theory for the dispersion of point sources (Taylor, 1922). Dispersion of particle clouds within the OSBL is dependent on both sheared mean currents and turbulence. When buoyant rise velocity is small, particle concentrations are transported vertically by turbulent eddies in all cases (ST, STBW, LT, LTBW). Within ST and STBW cases, mean currents are more sheared, resulting in differential advection of particle clouds with respect to depth. This results in larger turbulent diffusion coefficients for ST and STBW cases. In contrast, enhanced mixing due to LT results in more uniform currents with respect to depth. These currents do not as efficiently disperse particles along the horizontal plane and result in smaller turbulent diffusion coefficients for small buoyant rise velocities. Diffusion coefficients for BW cases are almost consistently smaller than for cases without BW effects due to both disruption of small scale coherent structures that efficiently disperse material by BWs (Kukulka and Brunner, 2015). As buoyant rise velocities increase, particles concentrate within near-surface regions. Small scale turbulence, generated within ST and STBW cases, is unable to efficiently submerge highly buoyant particles, resulting in largely reduced turbulent diffusion coefficients. Large scale Langmuir circulations still may submerge particles with relatively large buoyant rise velocity to regions with shear and relatively large turbulent eddies, enhancing shear dispersion and likely resulting in larger turbulent diffusion coefficients than ST/ STBW cases for large buoyant rise velocities.

To capture the effect of rotating currents with respect to depth within the Ekman layer, particle cloud dispersion statistics were calculated with respect to the principal axes of dispersion for all cases. Principal axes of dispersion are dependent on

both buoyant rise velocity and wave effects. Major and minor axes of dispersion are significantly misaligned with the direction of the wind for neutrally buoyant particles but align with wind direction as buoyant rise velocity is increased. Turbulent diffusion coefficients computed with respect to major and minor axes of dispersion are consistent with those observed for x and y axes. These results indicate that it is generally necessary to examine point source dispersion along the principal axes of dispersion.

Results of this study show that point source dispersion is dependent on both buoyant rise velocity and OSBL wave conditions. The applied Lagrangian method and coupled LES and Lagrangian stochastic model is an effective means for characterizing dispersion of buoyant particles within varying OSBL conditions.

REFERENCES

- Agrawal, Y. C., Terray, E. A., Donelan, M. A., Hwang, P.A., Williams, A. J., Drennan, W. M., Kahma, K. K., Krtaigorodskii, S. A., 1992. Enhanced dissipation of kinetic energy beneath surface waves. *Nature* 359, 219-220.
- Batchelor, G. K., 1950. The application of the similarity theory of turbulence to atmospheric diffusion. *Quarterly Journal of the Royal Meteorological Society* 76 (328), 133-146. URL <http://dx.doi.org/10.1002/qj.49707632804>
- Belcher, S.E., Grant, A. L. M., Hanley, K. E., Fox-Kemper, B., Van Roekel, L., Sullivan, P.P., Large, W. G., Brown, A., Hines, A., Calvert, D., Rutgersson, A., Pettersson, H., Bidlot, J.-R., Jannssen, P. A. E. M., Polton, J. A., 2012. A global perspective on Langmuir turbulence in the ocean surface boundary layer. *Geophys. Res. Lett.* 39)18), n/a – n/a. URL <http://dx.doi.org/10.1029/2012GL052932>
- Brunner, K., Kukulka, T., Proskurowski, G., Law, K. L., 2015. Passive buoyant tracers in the ocean surface boundary layer: 2. Observations and simulations of microplastic marine debris. *J. Geophys. Res. Oceans.* 120.
- Colbo, K., Li, M., 1999. Parameterizing particle dispersion in Langmuir circulation. *J. Geophys. Res.*, 104, 26059-26068.
- Craig, P. D., Banner, M. L., 1994. Modeling wave- enhanced turbulence in the ocean surface layer., *J. Phys. Oceanogr.* 24 (12), 2546-2559.
- Craik, A. D. D., Leibovich, S., 1976. A rational model for Langmuir circulations. *J. Fluid Mech.* 73, 401-426.
- Denman, K. L., Gargett, A. E., 1995. Biological physical interactions in the upper ocean: The role of vertical and small- scale transport processes. *Annu. Rev. Fluid Mech.* 27, 225-255.
- Denbo, D. W., Skyllingstad, E. D., 1995. An ocean large eddy simulation model with application to deep convection in the Greenland Sea. *J. Geophys. Res. Oceans.* 101. <https://doi.org/10.1029/95JC02828>
- Donelan, M. A., Hamilton, J., Hui, W. H., 1985. Directional spectra of wind-generated waves. *Philos. Trans. R. Soc. London, Ser. A* 315, 509-562.
- Farmer, D. M., Li, M., 1995. Patterns of bubble clouds organized by Langmuir circulation. *J. Phys. Oceanogr.* 25, 1425-1440.

Feynman, R. P., (Richard Phillips), 1918-1988. The Feynman Lectures on Physics. Reading, Mass. :Addison-Wesley Pub. Co., 1963/1965. Print.

Gill, A. E., 1982: Atmosphere- Ocean Dynamics. Academic Press, 662 pp.

Harcourt, R. R., and E. A. D'Asaro, 2008: Large eddy simulation of Langmuir turbulence in pure wind seas. *J. Phys. Oceanogr.*, 38, 1542–1562.

Kukulka, T., Brunner, K., 2015. Passive buoyant tracers in the ocean surface boundary layer: 1. Influence of equilibrium wind-waves on vertical distributions. *J. Geophys. Res. Oceans*. 120, 3837-3858.

Kukulka, T., Pleueddemann., A. J., Sullivan, P. P., 2012a. Nonlocal transport due to Langmuir circulations in a coastal ocean. *J. Geophys. Res.* 117.

Kukulka, T., Pleueddemann, A. J., Trowbridge, J. H., Sullivan, P. P., 2009. Significance of Langmuir circulation in upper ocean mixing. Comparison of observations and simulations. *Geophys. Res. Letter*. 36, doi:10.1029/2009GL037620.

Kukulka, T., A. Plueddemann, J. Trowbridge, and P. Sullivan (2011), The influence of crosswind tidal currents on Langmuir circulation in a shallow ocean, *J. Geophys. Res.*, 116, C08005, doi:10.1029/2011JC006971.

Kukulka, T., Plueddemann, A., Sullivan, P., 2013, Inhibited upper ocean restratification in nonequilibrium swell conditions, *Geophys. Res. Lett.*, 40, 1–5, doi:10.1002/grl.50708.

Kukulka, T., Veron, F., 2018. Lagrangian investigation of wave-driven turbulence in the ocean surface boundary layer.

Leibovich, S., 1983. The form and dynamics of Langmuir circulations. *Annu. Rev. Fluid. Mech.* 15, 391-427.

Li, M., Garret, C., Skillingstad, E., 2005. A regime diagram for classifying turbulent large eddies in the upper ocean. *Deep Sea Res. I* 52(2), 259-278.

Li, M., Vagle, S., Farmer, D. M., 2009. Large eddy simulations of upper- ocean response to a midlatitude storm and comparison with observations. *J. Phys. Oceanogr.* 29, 2295-2309.

Liang, J.-H., Emerson, S. R., D'Asaro, E. A., McNeil, C. L., Harcourt, R. R., Sullivan, P. P., Yang, B., Cronin, M. F., 2017. On the role of sea-state in bubble-mediated air-

sea gas flux during a winter storm. *Journal of Geophysical Research: Oceans* 122 (4), 2671-2685. URL <http://dx.doi.org/10.1002/2016JCO12408>

McWilliams, J. C., Sullivan, P. P., Moeng, C. H., 1997. Langmuir turbulence in the ocean. *J. Fluid Mech.* 334, 1-30.

McWilliams, J. C., Huckle, E., Liang, J.-H., 2013. Langmuir turbulence in swell. *J. Phys. Oceanogr.*, 44, 870-890. URL <https://doi.org/10.1175/JPO-D-13-0122.1>

Noh, Y., Kang, I. S., Herold, M., Raasch, S., 2006. Large eddy simulation of particle settling in the ocean and mixed layer. *Physics of Fluids* 18(8), 085109. URL <https://doi.org/10.1063/1.2337098>

Noh, Y., Min, H. S., Raasch, S., 2004. Large eddy simulation of the ocean mixed layer: The effects of wave breaking and Langmuir circulation. *J. Phys. Oceanogr.* 34 (4), 720-735.

Noh, Y., Nakada, S., 2010. Estimation of the particle flux from the convective mixed layer by large eddy simulation. *Journal of Geophysical Research: Oceans* 115 (C5), n/a – n/a. URL <http://dx.doi.org/10.1029/2009JC005669>

Polton, J. A., and S. E. Belcher, 2007: Langmuir turbulence and deeply penetrating jets in an unstratified mixed layer. *J. Geophys. Res.*, 112, C09020, doi:10.1029/2007JC004205.

Polton, J.A., D.M. Lewis, and S.E. Belcher, 2005: The Role of Wave-Induced Coriolis–Stokes Forcing on the Wind-Driven Mixed Layer. *J. Phys. Oceanogr.*, **35**, 444–457, <https://doi.org/10.1175/JPO2701.1>

Pope, S. B., 2008. *Turbulent flows*, 5th Edition. Cambridge University Press, Cambridge, UK.

Richardson, L. F., 1926. Atmospheric diffusion shown on a distance-neighbour graph. *Proceedings of the Royal Society of London A: Mathematical, Physical, and Engineering Sciences* 110 (756), 709-737. URL <http://rspa.royalsocietypublishing.org/content/110/756/709>

Sawford, B., 2001. Turbulent relative dispersion. *Annual Review of Fluid Mechanics* 33 (1), 289-317. URL <https://doi.org/10.1146/annurev.fluid.33.1.289>

Smith, J., Pinkel, R., Weller, R. A., 1987. Velocity structure in the mixed layer during MILDEX. *J. Phys. Oceanogr.* 17, 425-439.

- Sullivan, P. P., McWilliams, J. C., 2010. Dynamics of winds and currents coupled to surface waves. *Annu. Rev. Fluid Mech.* 42, 19-42.
- Sullivan, P. P., McWilliams, J. C., Melville, W. K., 2004. The oceanic boundary layer driven by wave breaking with stochastic variability. Part 1. Direct numerical simulations. *J. Fluid Mech.* 507, 143-174.
- Taylor, G. I., 1922. Diffusion by continuous movements. *Proc. London Math. Soc.* s2-20, 96-212.
- Taylor, G. I., 1953. Dispersion of soluble matter in solvent flowing slowly through a tube. *Proc. R. Soc. Lond. A* 1953 219 186-203; DOI: 10.1098/rspa.1953.0139. Published 25 August 1953
- Terray, E., Donelan, M., Agarwal, Y., Drennan, W., Kahma, K., Williams, A., Hwang, P., Kitaigorodskii, S., 1996. Estimates of kinetic energy dissipation under breaking waves. *J. Phys. Oceanogr.* 26, 792-807.
- Thorpe, S. A., 2004. Langmuir circulation, *Annu. Rev. Fluid Mech.* 36, 55-79.
- Thorpe, S.A., Osborn, T.R., Jackson, J. F. E., Hall, A.J., Lueck, R. G., 2003a. Measurements of turbulence in the upper ocean mixing layer using Autosub. *J. Phys. Oceanogr.* 3, 122–145
- Thorpe, S. A., Osborn, T.R., Farmer, D.M., Vagel, S., 2003b. Bubble clouds and Langmuir circulation: observations and models. *J. Phys. Oceanogr.* 33, 2013–2031
- Weller, R. A., and J. F. Price, 1988: Langmuir circulation within the oceanic mixed layer. *Deep-Sea Res.*, 35, 711–747.
- Weil, J. C., Sullivan, P. P., Moeng, C.-H., 2004. The use of large-eddy simulations in lagrangian particle dispersion models. *J. Atmos. Sci.* 61, 2877-2887.
- Yang, D., Chamecki, M., Meneveau, C., 2014. Inhibition of oil plume dilution in Langmuir ocean circulation. *Geophysical Research Letters* 41 (5), 1632-1638. URL <http://dx.doi.org/10.1002/2014GL059284>